Reconfigurable Microstrip Filter with Continuous Coupling and Frequency Tunability

by

Alwyn Petrus Kotzé

Thesis presented in fulfilment of the

requirements for the degree of

Masters of Engineering (Electronic)

in the Faculty of Engineering at Stellenbosch University

Supervisors: Dr. E. Meyer
Prof. P. Meyer

December 2021

Declaration

By submitting this thesis electronically, I declare that the entirety of the work contained therein is my own, original work, that I am the sole author thereof (save to the extent explicitly otherwise stated), that reproduction and publication thereof by Stellenbosch University will not infringe any third party rights and that I have not previously in its entirety or in part submitted it for obtaining any qualification.

Date: December 2021

Abstract

For the modern communication system, adaptability is an essential requirement to remain relevant in the current day and age. This project focuses on the implementation of a varactor structure to provide a method of controlling the coupling in coupled-resonator filters. This will allow a single filter to preform the task of multiple set bandwidth filters and allow a single filter to adapt to new requirements when needed. The coupling structure in this project is used to limit the magnetic coupling strength so that the dominant coupling type is electrical and uses the structure placement and choice of resonator to achieve the required tuning range. The coupling structure can control the pass-band bandwidth to change from 300 MHz to 600 MHz with a center frequency tuning range of 2 -3.5 GHz and 3.36 to 2.75 GHz. This project uses ideal transmission line models and simulation software like CST and AWR to determine the characteristics of the filter. The coupling structure adds an insertion loss zero and pole. By means of good design choices the pole can limit the zeros' influence on the pass-band. Measurements show that the models predicted the characteristics with good accuracy, however an increase in loss due to the varactor is observed in measurement. The project did show that the use of the varactor structure provides a good method of controlling the coupling strength.

Opsommings

Vir die moderne kommunikasiestelsel is aanpasbaarheid 'n noodsaaklike vereiste om op die huidige tyd relevant te bly. Die projek fokus op die implementering van 'n varaktorstruktuur om 'n metode te bied om die koppelsterkte in gekoppelde resonerende filter te beheer. Die koppelstruktuur word gebruik om die magnetiese koppelsterkte te beperk sodat die dominante koppelingstipe elektries is. Die invloed van die plasing van die koppelstruktuur op 'n mikrostrook resoneerder sal getoets en bespreek word om te bepaal wat nodig is vir 'n spesifieke verstelbaarheid. Die koppelstruktuur kan die deurlaatband reguleer om van 300 MHz na 600 MHz met die middel frekwensie verstelbarheid van 2 -3.5 GHz en 3.36 to 2.75 GHz. Hierdie projek maak gebruik van ideale transmissielyn modelle en simulasiesagteware soos CST en AWR om die eienskappe van die filter akkuraat te bepaal. Die koppelstruktuur wys dat dit 'n invoegverlies zero en pool toevoeg, en met goeie ontwerpkeuses kan die pole die invloed van die zero op die deurlaatband beperk. Metings toon dat die modelle die eienskappe met goeie akkuraatheid voorspel het, maar as gevolg van die varaktormodel wat vir hierdie projek gebruik word, is die verlies meer in werklikheid as in simulasie. Die projek het getoon dat die gebruik van die varaktorstruktuur 'n goeie metode bied om die koppelsterkte te beheer.

Acknowledgements

I would like to acknowledge the contribution of the following people and organization that helped this project

- Prof. Meyer and Dr. Meyer for their input and wisdom.
- My wife Mariska for here support and constant words of encouragement.
- My parents and siblings for their support.
- National Research Foundation (NRF) and Department of Electrical and Electronic Engineering, SU, for the financial assistance.
- Wessel Croukamp and Wynand van Eeden for manufacturing the filter.
- Ms. Anneke Bester for helping me with the measurements.

Contents

List of Figures

List of Tables

Chapter 1

Introduction

This chapter introduces the problem addressed by this project, outlines the project goals, and describes the layout of this thesis.

1.1 Filter Development

Modern communication technology originates from knowledge developed during the second world war [7]. From this time period the researchers have developed methods of miniaturization and cost reduction. Different communication standards and bandwidth regulations are set in place to allow companies and countries to develop and use the available spectrum for communication and products. Modern communication technologies require higher flexibility for the current method of communication. Filter banks are one of these solutions where multiple filters provide high isolation between allotted bandwidths [8]. This leads to large structures and is not a practical solution for systems where mobility is a priority. The development of tunable filters allowed the reduction in the number of filters required.

The potential use of adjustable filters is not limited by only the reduction of size requirements but also the improvement of system performance by changing the pass-band as needed. Additionally if the characteristics of a filter is known it can be used to isolate and monitor multiple communications channels. This can be done by having pre-selected values the components can be set and each set is a difference channel pass-band.

With the recent implementation of the 5G communication standard, a potential use of adjustable filters can be argued due to the large changes of the allocated spectrum due to the reserved bandwidths for the new communication standard. The use of adjustable filters can extend the relevancy of a system by allowing the pass-band to change to fit the regulations and thus extending the system life cycle by being able to adapt. Naturally this is only possible if the changes in regulation are within the range of the system.

However the larger the tuning range the more difficult it is to maintain a good filter response, due to physical limitations of the components [9]. The implementation of tunablity was achieved by using materials like Yttruim-Iron-Granet (YIG) and Barium Strontuim Titanate (BST) and changing the current or voltage the resonant frequency can be altered [9]. A common method of designing continuous tunable filters is with the use of Micro-Electro-Mechanical systems (MEMS) or varactor diodes on existing filter typologies to manipulate the electrical length of resonators to shift the center frequency of the filter [10, 6, 11, 12, 13].

1.2 Published Work

Methods for achieving coupling variability have been widely researched on planar topologies [1][2] [3]. Each approach used an unique method om implementing an electronic controlled coupling. For the purpose of this study, methods using varactor are used due to the availability of varactors and ease of implementation.

1.2.1 Non-Resonant Node Inverter

The method used in [1] makes use of an additional resonator to manipulate the coupling between adjacent resonators. The filter in Fig. 1.1 shows where the additional resonator is placed and is label as NRN for non-resonant node. This naming convention is due to this resonator's resonant frequency are high enough that it does not influence the pass-band but it can be used to manipulate the coupling strength.

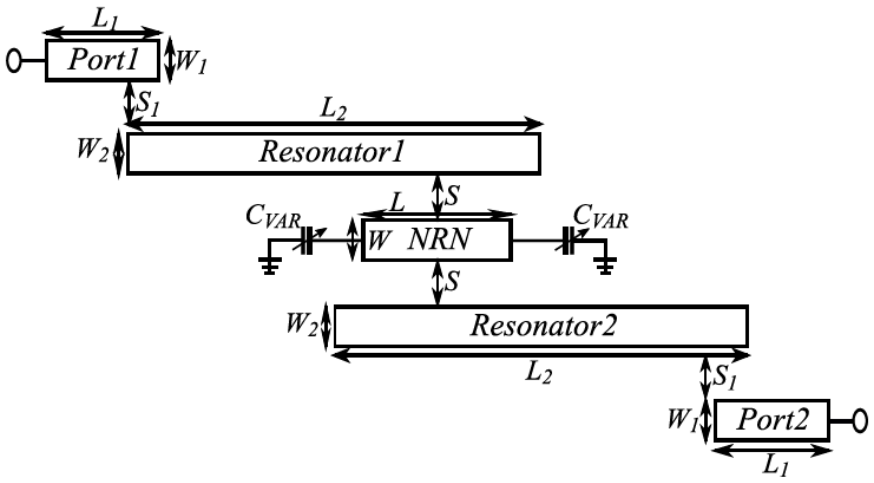

Figure 1.1: Coupling tuning using non-resonant node inverter

Sharma shows that the coupling model can be represented by the circuit model in Fig. 1.2(a) where the coupling towards the NRN is represented by a pi-network [1]. This model simplifies through the use of varactor capacitance (represented jB'_{var}) that cancel the influence of the coupling has on the NRN and reduces the circuit in Fig. 1.2(a) to that shown in Fig. 1.2(b). This reduced circuit manipulates the coupling strength by manipulating the electrical length of the NRN which is controlled by the excess capacitance provided by the varactor. The transmission line in Fig. 1.2(b) (labeled as T_{LC}) is used to represent the transmission line in Fig. 1.2(a) (labeled as T_{LB}) and the influence $jB'_{var} - jB'$ has on it.

To allow this circuit to have the characteristics of an inverter the new pi-network model's ABCD matrix is equated to that of a standard pi-network inverter ABCD matrix. Using this method Sharama provides equations that express the coupling strength in terms of jB and jB' as shown in Eqn. 1.2.1. The resonator slope parameter is represented as β, when adjacent pass-band resonators are identical.

$$k = \frac{B'^2(2B_{var}cos\theta Y'_0 + B^2_{var}sin\theta' + Y'^2_0 sin\theta')}{Y'_0 Y^2_0 \beta} \tag{1.2.1}$$

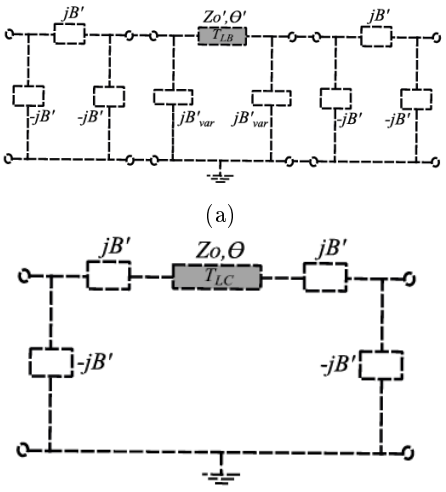

Figure 1.2: NI circuit model [1]

Using the filter model Sharama provides simulated results that provide insight on the influence this coupling structure has on the filter response. Fig. 1.3 is the simulated S_{21} response of the filter in Fig. 1.1 using the equations provided by Sharama in [1] to design the filter. The results show that the using the NRN introduces an insertion loss zero to the response above the pass-band. The frequency of this zero is controlled by the electrical length of the NRN.

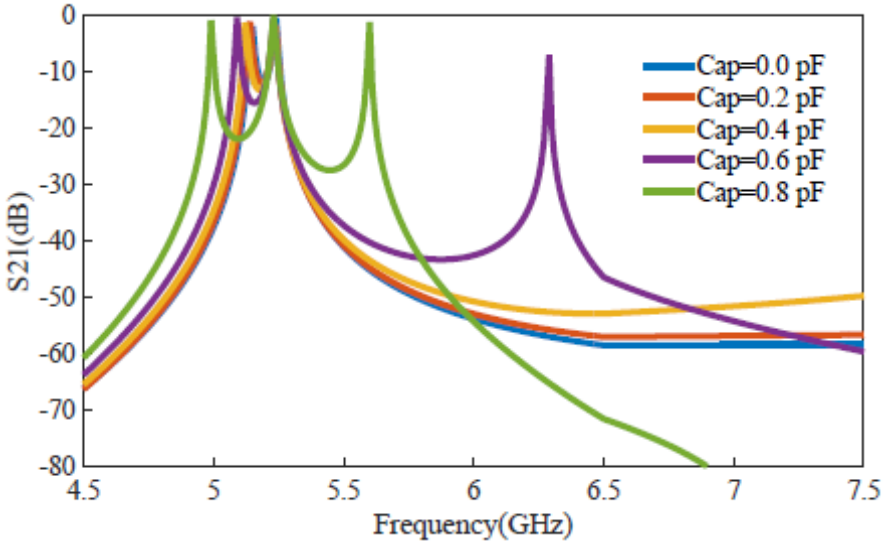

Figure 1.3: Simulated S_{21} response of a second order filter

The NRN provides a functional method of manipulating the coupling strength of a filter and with the correct design choices the additional insertion loss zero's influence can be reduced by placement of the zero far enough above the pass-band.

1.2.2 Coupling Reducer

The varactor structure in Fig. 1.4 is the adaptation of a combline filter to control the coupling strength of a filter by limiting the growth of the coupling as the center-frequency shifts [2].

This method is used to provide a constant bandwidth by using the known characteristics of the coupling coefficient of the combline filter to control the coupling strength [14]. This is done by manipulating the electrical coupling of the combline filter with the use of an adjustable capacitance load.

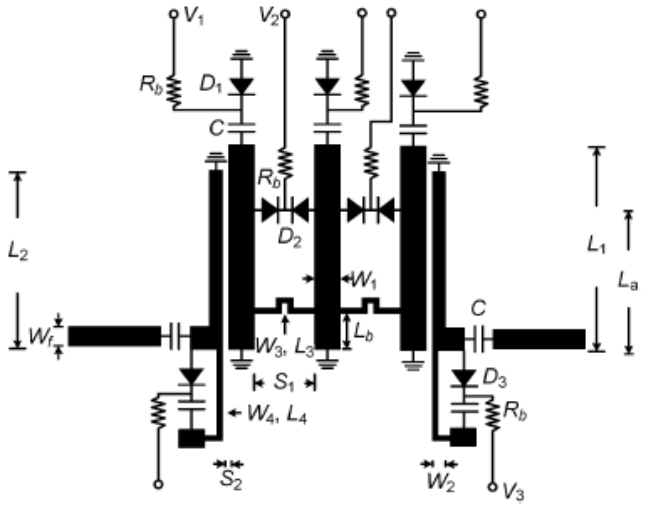

Figure 1.4: Combline filter with varactor structures to control coupling strength

The transmission line labeled Y_a (shown in Fig 1.5) represents the natural coupling between adjacent resonators. The analysis of the coupling structure is done by using even and odd mode conditions that manipulate the circuit model shown in Fig. 1.5(a) to provide the models shown in Fig. 1.5(b). Using the even and odd mode the equivalent resonant frequencies can be derived and used to determine the coupling strength as shown in Eqn. 1.2.2 [2].

$$k = \frac{f_{or}^2 - f_{er}^2}{f_{or}^2 + f_{er}^2} = \frac{\Delta}{\sqrt{g_1 g_2}} \tag{1.2.2}$$

The simulated result shown in Fig. 1.6 indicates that the use of this structure provides an adequate method of controlling the coupling strength and maintains a constant bandwidth with the range of approximately 1 GHz. The bi-variant study shown in Fig. 1.7 indicates the bandwidth range at different fixed C_1 and C_2 values. Additionally this study provided by [2] shows the influence transmission line length labeled L_3 has on the bandwidth range. The data set where L_3 is set to zero indicates where [2] removed the transmission line completely.

The results in Fig. 1.7 provides proof that without an element that increases the magnetic coupling the minimum value of the varactor reduces the total coupling strength to the point that the bandwidth range is substantially reduced. The use of the back to back varactor structure also restricts spacing between resonators, meaning that the only method of increasing the total coupling strength is with the use of L_3.

1.2.3 T-type Bandwidth Control Structure

The T-type structure is used in [3] to change the dominant coupling method of a combline filter from magnetic to electric. This method, in contrast to the method shown in [2], uses

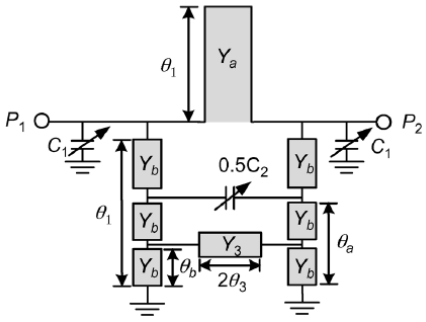

(a) Circuit model

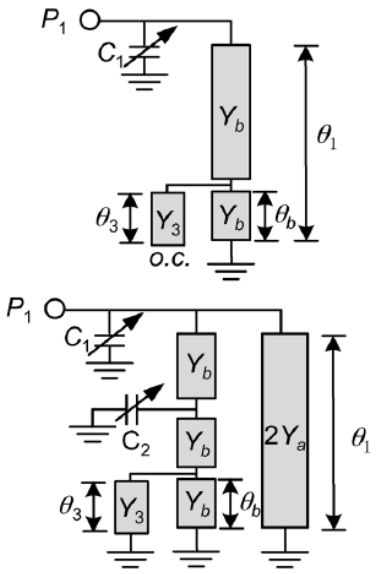

(b) Even and odd mode circuit model

Figure 1.5: Coupling reducing circuit diagram [2]

the varactor structure to control the dominant coupling method. For this study the coupling between source and load was ignored and focus was on the coupling structure used in [3] to control K_{12}. The purpose of C_3 is to reduce the total coupling strength to be able to design narrow band filters with this structure [3].

The even and odd mode evaluation between adjacent resonators lead to the circuits shown in Fig. 1.9. Using the even and odd mode analyses [3] shows that the coupling coefficient K_{12} can be expressed as Eqn. 1.2.5 when $L_1 = L_3$.

$$K_{12} = \frac{\frac{IM[Y_{in,e}(\omega_0) - Y_{in,o}(\omega_0)]}{2}}{b} \tag{1.2.3}$$

$$b = \frac{\omega_0}{2} \frac{\delta IM[\frac{[Y_{in,e} - Y_{in,o}]}{2}]}{\delta\omega}|_{\omega=\omega_0} \tag{1.2.4}$$

$$K_{12} = 2\frac{(Y_{0o} - Y_{0e})cot\beta l1 + \omega_0 C_2(\frac{C_3}{C_3+2C_2} - 1)}{(Y_{0o} + Y_{0e})[\beta L_1 csc^2(\beta L_1) + cot\beta L_1]} \tag{1.2.5}$$

The simulated results shown in Fig 1.10 provides evidence that the T-type structure provides a constant bandwidth with a range of 1 GHz.

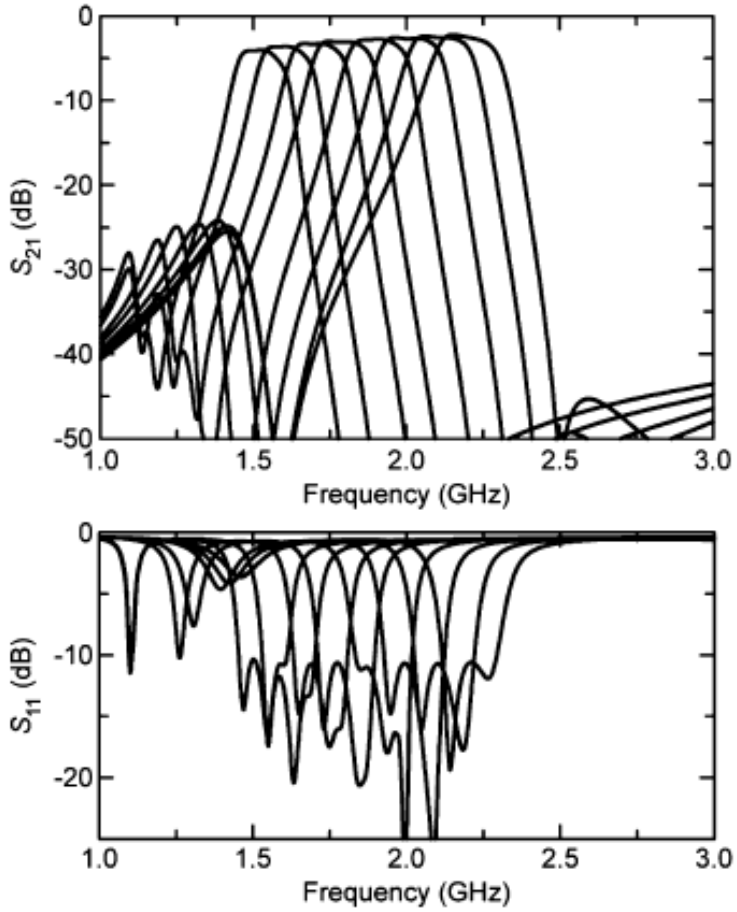

Figure 1.6: Simulated S_{11} and S_{21} response [2]

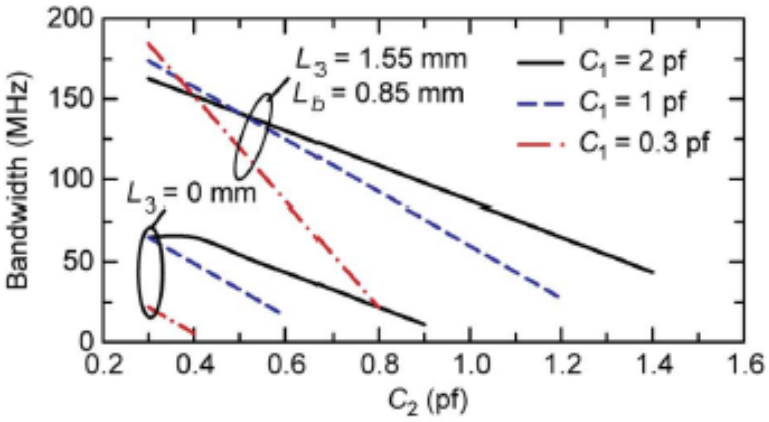

Figure 1.7: Simulated Bi-variant bandwidth study

Further investigation by [3] shows that using this coupling control that both a 35 and 100 MHz bandwidth can be maintained over a large frequency range. The data set in Fig. 1.11(a) show that without any change in C_2 and $C_3 = 0$ the range of the coupling coefficient is large and directly proportional to the frequency. This is the opposite of what is required because to maintain an absolute bandwidth the coupling coefficient must be inversely perceptional [3].

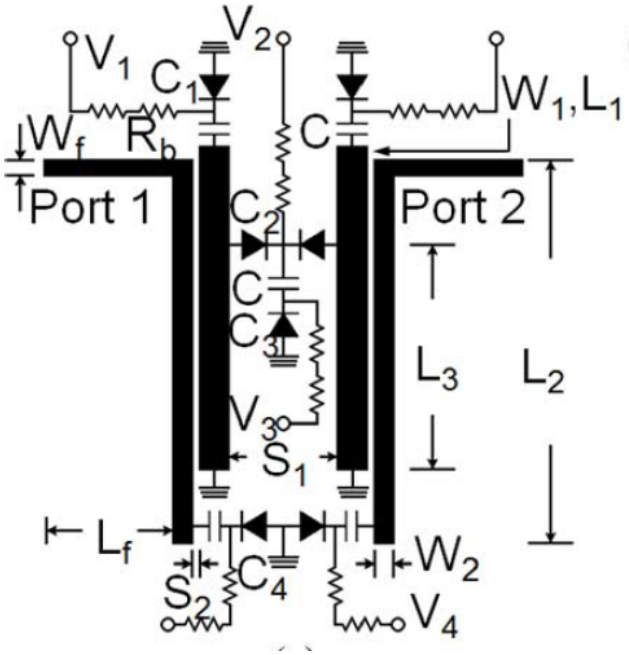

Figure 1.8: Microstrip filter implementing T-type coupling control [3]

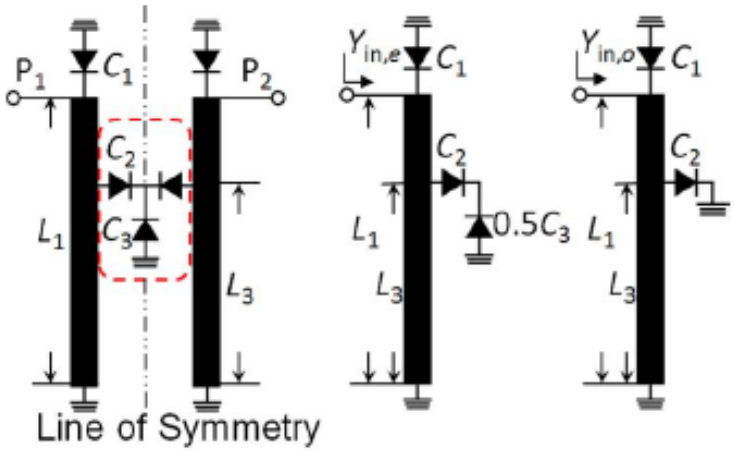

Figure 1.9: T-type even and odd mode analysis[3]

1.3 Problem Statement

This project will focus on developing a filter structure that can be used in a wider range of communication systems. Reconfigurable filter structures are developed to provide a method of adjusting to the needs of a system, through the change in the center frequency or the bandwidth allotted to the communication system. The functional advantage of using a reconfigurable/adjustable filter is that the filter has the potential for reducing the total size of the communication system and the filter has the potential to remain relevant even after a communication standard changes [1]. The cost of using a filter that does not specialize in a single bandwidth is that the response will never be better than a fixed bandwidth filter.

The filter shown in Fig. 1.4 shows the use of a classic combline filter topology, shown in Fig. 1.12, as base line structure to implement coupling tunability [2].

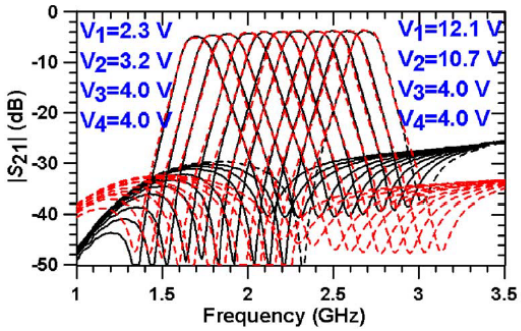

(a) S_{21}

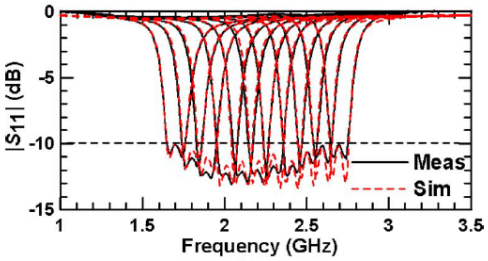

(b) S_11

Figure 1.10: Simulated S parameter response [3]

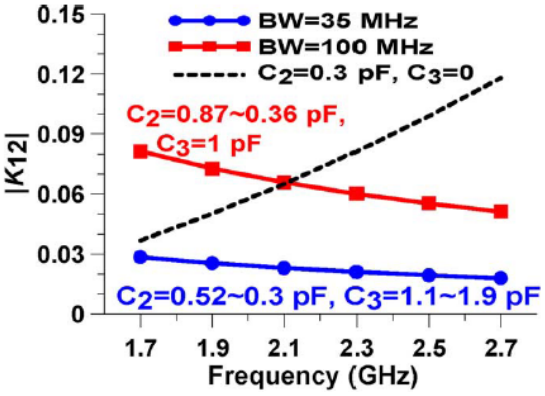

(a) Coupling coefficient vs Frequency

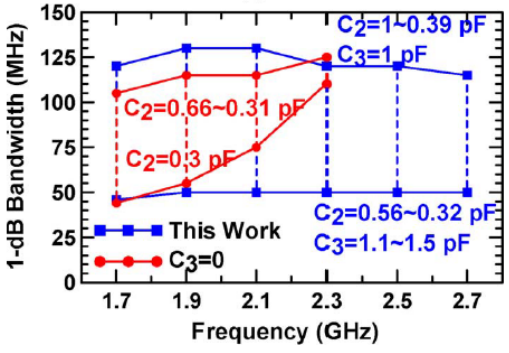

(b) 1 dB bandwidth vs frequency

Figure 1.11: Simulated results to maintain a constant bandwidth [3]

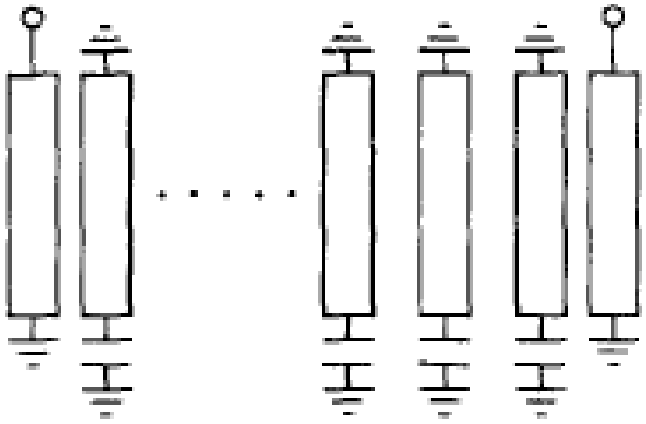

Figure 1.12: Combline filter

The advantage of using a combline filter as a base structure is the symmetrical nature of the coupling as the magnetic fields show in Fig 1.13. The symmetry means that a coupling structure influences adjacent resonators symmetric as well. This is shown in the filter design in Fig. 1.4 with the symmetric placement of the varactor and transmission line structure (D2 and L3 shown in Fig. 1.4).

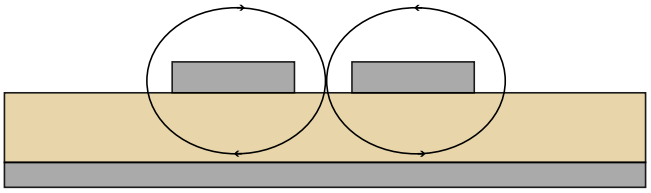

Figure 1.13: Broadside magnetic coupling between adjacent conductors

The disadvantage of using a combline structure as a base structure to design adjustable a filter is that the shifting the center frequency influences the strength of the magnetic coupling shown in Fig. 1.13 and the coupling tunability must adjust to maintain a constant absolute bandwidth. The commonly used adjustable components are capacitors and due to the properties of combline structures the electrical and magnetic coupling act destructive towards to the totals coupling strength.

Due to these disadvantages filter designs use adjustable capacitors to either influence the coupling indirectly via a NRN, limit the coupling growth of a combline structure or use the adjustable capacitance to increase the electric coupling of the filter so that electric coupling is the dominant form of coupling.

This project will focus on a similar design as shown in both [2] and [3]. The structure will use a transmission line to decrease the magnetic coupling between resonators and use a varactor structure to provide electrical coupling as shown in Fig. 1.14. This project will design a model and determine the influence of the coupling structure on the filter response. This model will be used to design a 3rde order filter with at 1 GHz center frequency tuning range whilst maintaining a constant bandwidth. Additional tests will be run to determine the range of pass-bands and see how far each pass-band can be shifted.

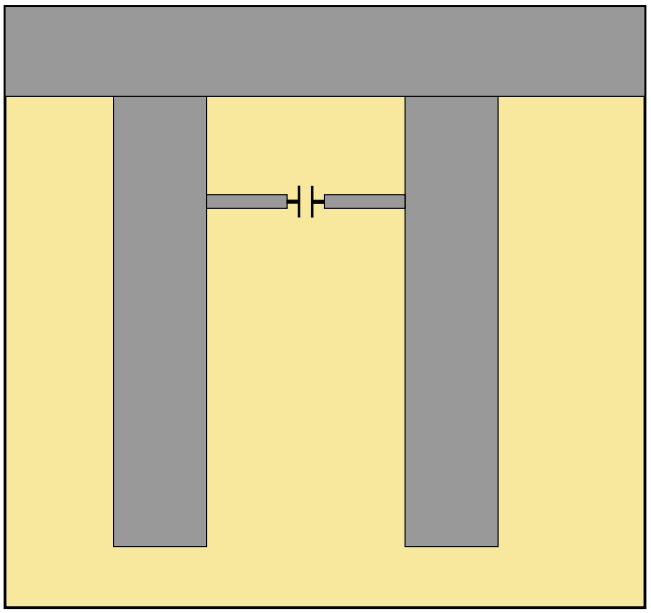

Figure 1.14: Coupling tuning using varactor bridge

1.4 Thesis Layout

Chapter 2 elaborates on the topics of filter fundamentals starting from the prototype used to decide the optimal response of the filter, ideal filter transformations with and without inverter components, the mechanisms of coupling and how it is represented in a filter, different topologies and how each works and components used to implement tunability. Chapter 3 will discuss the ideal implementation of coupling tunability this project uses, how the solution impacts ideal transmission lines and the design of a microstrip filter. Chapter 4 discusses the in-house manufacturing and the results.

Chapter 2

Filter Fundamentals

In this chapter the basic filter theory necessary for coupled resonator filter design is provided. Commonly-used filter synthesis methods, low-pass prototype design by means of the insertion loss parameter, definitions of important figures of merit, as well as tools for transforming the prototype to a coupled resonator filter model are included. Lastly, different coupled resonator filter topologies and electrically tunable component options are discussed.

2.1 Network Synthesis Method

The network synthesis method is also known as the insertion loss method. It is the method by which a response is described in terms of the power available from the source (P_{inc}) divided by the power delivered to the load (P_{load}) as shown in eq. 2.1.1. This relationship is known as the power loss ratio (P_{LR}) [15].

$$P_{LR} = \frac{P_{inc}}{P_{load}} = \frac{1}{|S_{12}|^2} \tag{2.1.1}$$

For P_{LR} to be physically realizable it must be in the form of eq. 2.1.2 that has two real polynomials in ω^2 denoted as $N(\omega^2)$ and $M(\omega^2)$ [15].

$$P_{LR} = 1 + \frac{M(\omega^2)}{N(\omega^2)} \tag{2.1.2}$$

The relationship shown in eq. 2.1.3 shows how insertion loss (IL) is related to P_{LR} in the dB scale.

$$IL = 10\log(P_{LR}) \tag{2.1.3}$$

Each transfer function uses different polynomials to describe P_{LR} and each function is designed to prioritize different characteristics.

2.1.1 Transfer Functions

The four well-known transfer functions used when designing filters are the Butterworth, Linear Phase, Elliptic, and Chebychev responses.

The Butterworth response provides an optimally flat pass-band response. The response is primarily used when a sharp response in the rejection band is not the dominant critical requirement but the flatness of the response is [15].

The Linear Phase is a response where the distortion of a signal needs to be minimized to improve the detection of the signal. The downside of a filter that is designed to minimize the effect of the phase of the signal is that the attenuation response has a more gradual increase when compared to other filter responses [15].

The Elliptic response focuses on equi-ripple in both the stop-band a pass-band. This comes with the downside of being more complex to synthesize [15].

The Chebychev (or equal ripple) response is known for its sharp increasing insertion loss in the stop-band, providing high isolation between adjacent channels [15].

Given that this project is focused on communication systems and it is acceptable to use a Chebychev response with a low ripple, a Chebychev response is chosen for its fast roll-off, allowing for channel selection with a low order filter.

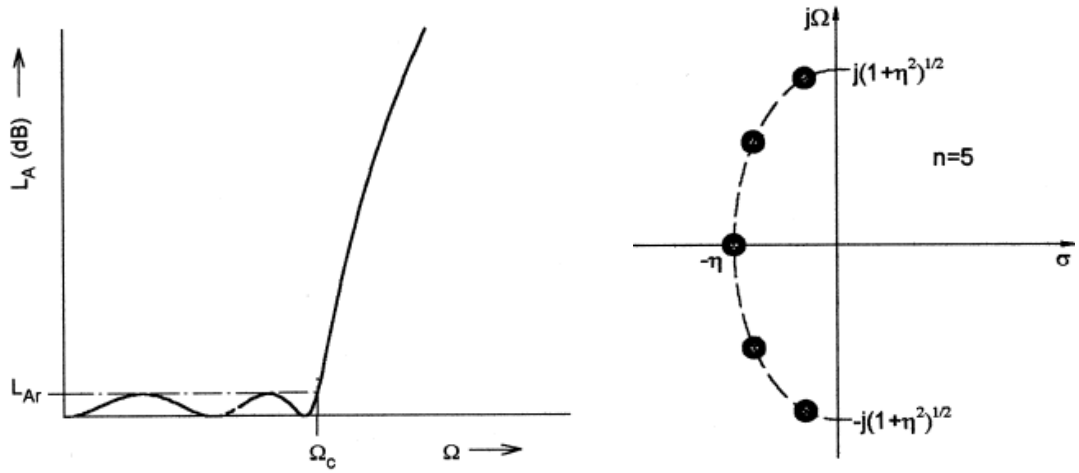

(a) Chebyshev response insertion loss for prototype

(b) Zero positioning of the Chebychev response in the complex frequency domain

Figure 2.1: Chebyshev properties [4]

The Chebychev response is known as an all pole response where the only zeros exist at zero and infinity for band-pass filters. The relationship between the insertion loss and transfer function is established in eq. 2.1.3.

$$\beta = \ln(\coth(\frac{IL_{pb}}{17.37})) \tag{2.1.4}$$

$$\gamma = \sinh(\frac{\beta}{2n}) \tag{2.1.5}$$

$$a_k = \sin[\frac{(2k-1)\pi}{2n}] \text{ , k = 1,2,3,...,n} \tag{2.1.6}$$

$$b_k = \gamma^2 + \sin^2(\frac{k\pi}{n}) \text{ , k = 1,2,3,...,n} \tag{2.1.7}$$

$$g_1 = \frac{2a_1}{\gamma} \tag{2.1.8}$$

$$g_k = \frac{4a_{k-1}a_k}{b_{k-1}g_{k-1}} \tag{2.1.9}$$

$$g_{n+1} = \begin{cases} 1 & \text{n odd} \\ \coth^2(\frac{\beta}{4}) & \text{n even} \end{cases} \tag{2.1.10}$$

IL_{pb} represents the insertion loss in the pass-band.

Using the equations from [5] shown in eq. 2.1.4-2.1.10 the low-pass prototype element values (g_n) can be extracted.

2.2 Low-pass Prototypes

Regardless of the transfer function chosen for an in-line filter, the low-pass prototype element values (labeled g_0 to g_{n+1} in Fig. 2.2 and 2.3) can be extracted. The element values are normalized to the source impedance of 1 Ω, while the filter has a cut-off frequency of $\omega_c = 1$. The ladder circuit consists of series inductance and shunt capacitance that can be in any of the circuit layouts in Fig. 2.2 and 2.3 [5].

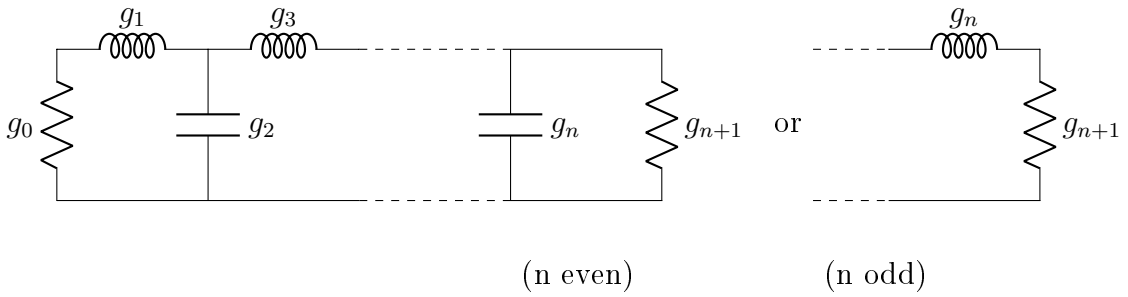

Figure 2.2: Low-pass lumped element ladder circuit with a initial series component

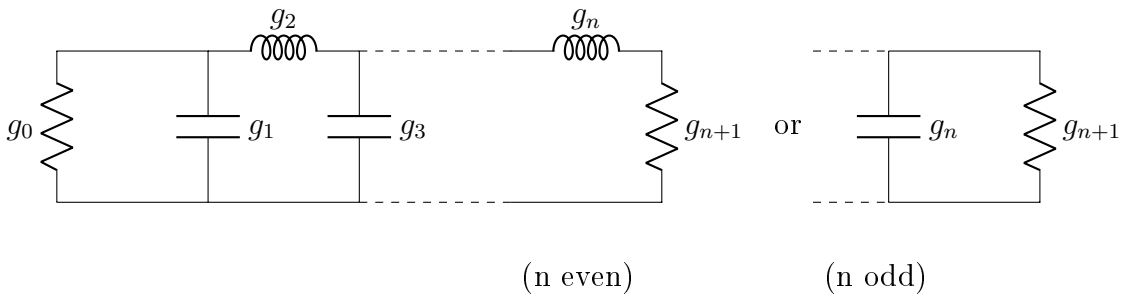

Figure 2.3: Low-pass lumped element ladder circuit with a initial parallel component

The element values, shown in Fig. 2.3 and 2.2, are generic variables that remain the same regardless of the ladder circuit chosen. The elements denoted g_0 and g_{n+1} are the source and load respectively and n is the order of the filter.

2.3 Band-pass Prototype

The low-pass prototype can be transformed into a band-stop, high-pass and band-pass filter. However a band-pass filter is the most suited to channel selection. In order to achieve a realizable band-pass filter, a series of transformations or manipulations need to be applied to the low-pass prototype circuit. Impedance and frequency scaling, low-pass to bandpass transformation, and circuit manipulations using impedance inverters are most often used.

2.3.1 Impedance Scaling

The low-pass prototype source impedance is 1Ω and the circuit must be scaled.

$$L_n^{'} = R_0 g_i \text{ for i = 1 to n} \tag{2.3.1}$$

$$C_n^{'} = \frac{g_i}{R_0} \text{ for i = 1 to n} \tag{2.3.2}$$

$$R_s^{'} = g_0 R_0 \tag{2.3.3}$$

$$R_L^{'} = g_{n+1} R_0 \tag{2.3.4}$$

The terms $L_n^{'}$, $C_n^{'}$, $R_s^{'}$ and $R_L^{'}$ in eq. 2.3.1 - 2.3.4 are the impedance scaled low-pass filter element values [15]. $R_s^{'}$ and $R_L^{'}$ represent the source and load. $L_n^{'}$ and $C_n^{'}$ represent the reactive elements of the circuit. The use of $L_n^{'}$ and $C_n^{'}$ will be dependent on whether the g_n is allocated to a series inductor or shunt capacitor.

2.3.2 Frequency and Scaling

The first step to transform a low-pass filter to a band-pass filter is by determining the maximum (ω_2) and minimum (ω_1) frequencies of the band. The center frequency (ω_0) and fractional bandwidth (Δ) can be determined as shown in eq. 2.3.5 and 2.3.6 [15].

$$\omega_0 = \sqrt{\omega_2 \omega_1} \tag{2.3.5}$$

$$\Delta = \frac{\omega_2 - \omega_1}{\omega_0} \tag{2.3.6}$$

The low-pass prototype can be scaled as shown below.

$$L_n^{''} = \frac{L_n^{'}}{\Delta} \tag{2.3.7}$$

$$C_n^{''} = \frac{Cn^{'}}{\Delta} \tag{2.3.8}$$

The final step to create a band-pass ideal lumped element filter is substituting as follows.

$$\omega \leftarrow \frac{\omega}{\omega_0} - \frac{\omega_0}{\omega} \tag{2.3.9}$$

This allows all the reactance/susceptance of the series inductors/shunt capacitors to be equated to the reactance/susceptance of the series/parallel resonators. The insertion loss is mapped to the band-pass filter [15].

$$jX = j(\frac{\omega}{\omega_0} - \frac{\omega_0}{\omega})L'' = j\omega L_S^{BP} - \frac{j}{\omega C_S^{BP}} \tag{2.3.10}$$

$$jB = j(\frac{\omega}{\omega_0} - \frac{\omega_0}{\omega})L'' = j\omega L_P^{BP} - \frac{j}{\omega C_P^{BP}} \tag{2.3.11}$$

By simplifying each of the equations the band-pass ideal lumped-element equivalent circuit can be derived in terms of the low-pass ideal lumped-element values [15].

$$L_s^{BP} = \frac{L_n''}{\omega_0} \tag{2.3.12}$$

$$C_s^{BP} = \frac{1}{\omega_0 L_n''} \tag{2.3.13}$$

$$L_p^{BP} = \frac{1}{\omega_0 C_n'''} \tag{2.3.14}$$

$$C_p^{BP} = \frac{C_n''}{\omega_0} \tag{2.3.15}$$

The simplified equations provide a set of reactive elements to use in series and parallel as seen in Fig. 2.4.

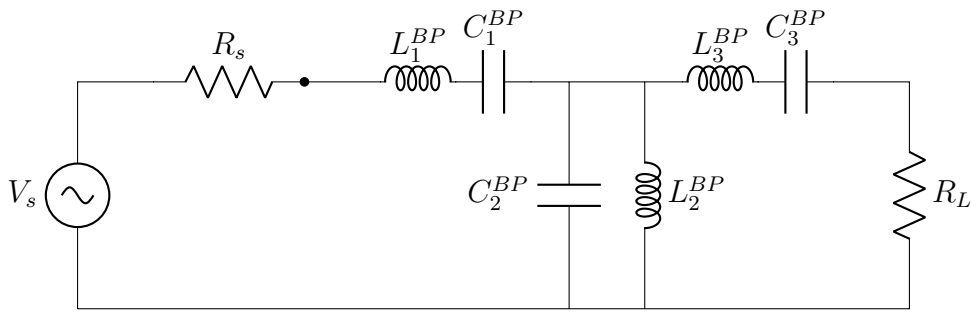

Figure 2.4: Ideal lumped element band-pass filter

Component values derived at high frequencies can be extremely small, so lumped element components cannot be produced with these small values. However it is possible to create filters that use distributed elements and keep the use of lumped-elements to a minimum.

2.3.3 Inverters

The idea of an inverter is to transform the impedance of a load to a preferred impedance. Using inverters, it is possible to transform the circuit in Fig. 2.4 into a circuit with "n" identical resonators. This reduces the amount of filter variables.

The ideal form of an inverter is a symmetrical two port network that transforms the load and adds a phase shift of ±90 degrees [5]. The ABCD matrices for an impedance and admittance inverter are given in eq.2.3.16 and 2.3.17, respectively. This means that any circuit used to

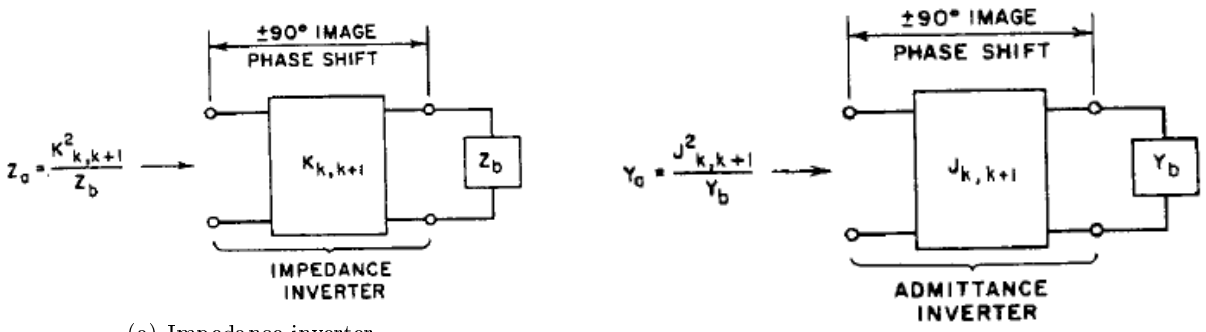

(a) Impedance inverter

(b) Admittance inverter

Figure 2.5: Ideal representation of inverters[5]

represent the inverter must have these characteristics at the frequency the inverter is used [5]. The simplest example of an inverter is a quarter wavelength transmission line.

$$\begin{bmatrix} A & B \\ C & D \end{bmatrix} = \begin{bmatrix} 0 & \pm\frac{1}{K} \\ \mp K & 0 \end{bmatrix} \tag{2.3.16}$$

$$\begin{bmatrix} A & B \\ C & D \end{bmatrix} = \begin{bmatrix} 0 & \pm\frac{1}{J} \\ \mp J & 0 \end{bmatrix} \tag{2.3.17}$$

An ideal inverter as shown in Fig. 2.5 is an inverter that would have the same inverter constant at all frequencies. This is impossible due to the physical limitations of components used to design inverter circuits.

(a) Impedance lumped inverter

(b) Admittance lumped inverter

Figure 2.6: Inverter implementation

The circuits in Fig. 2.6 show one available option for each inverter type. All the circuits shown in Fig. 2.6 share the problem of only being an ideal inverter at one frequency [4].

2.4 Q-Factor

The quality factor (Q-factor) characterizes the ability of a resonator to store energy. In eq. 2.4.1 the quality factor is the ratio of average stored energy in the electric and magnetic fields (W_{stored}), and the total energy loss (P_{loss}) of the resonator [15].

$$Q = \omega_0 \frac{W_{stored}}{P_{loss}} = \omega_0 \frac{W_m - W_e}{P_{loss}} = \omega_0 \frac{2W_m}{P_{loss}} = \omega_0 \frac{2W_e}{P_{loss}} \quad \text{at resonance} \tag{2.4.1}$$

To establish an accurate value for each component of eq. 2.4.1 is not simple and an EM solution for a resonator is time consuming. To simplify the problem a RLC circuit model is used as a reasonably accurate narrow band model for different resonator types.

(a) Parallel resonator

(b) Series resonator

Figure 2.7: Simplified RLC circuit resonator models

When a resonator is simplified to RLC as presented in Fig. 2.7, the input impedance for the series circuit is $Z_{in} = R + j\omega L - j\frac{1}{\omega C}$, and $Z_{in} = (G + j\omega C - j\frac{1}{\omega L})^{-1}$ for the parallel circuit.

When a resonator functions at resonance, the energy stored is equally distributed between the magnetic field and the electric field, meaning that in the simplified circuits in Fig. 2.7 the inductive and capacitive component cancel out at resonance. Therefore, at resonance, $Z_{in}(\omega_0)$ is only a real load. The total average energy stored in a resonator can be described as double the average energy stored in the electric or magnetic field of the resonator [15]. Using resonators with low Q values results in increased loss and decreased selectivity in the filter response. [5].

2.4.1 Loaded Q

In the practical application of resonators energy must be provided. This introduces external elements that affect the unloaded response of a resonator.

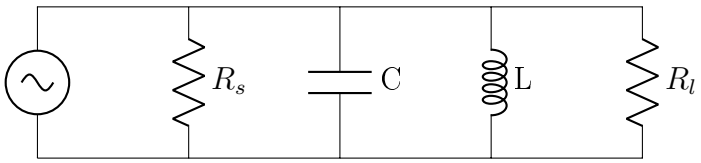

(a) Loaded Quality factor Paralle circuit

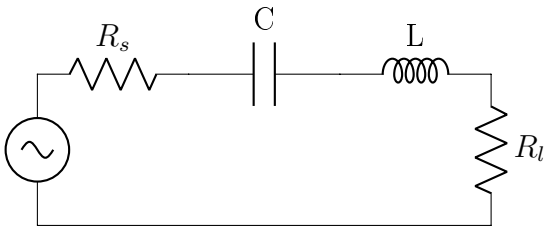

(b) Loaded Quality factor Series circuit

Figure 2.8: Simplified RLC loaded resonator

The loaded quality factor is a result of the external and unloaded quality factors, as shown in eq 2.4.2

$$Q_L = \begin{cases} \frac{\omega_0 L}{R_l + R_s} & \text{Series resonator} \\ \frac{R_s R_l}{\omega_0 L[R_L + R_s]} & \text{Parallel Resonator} \end{cases} \tag{2.4.2}$$

$$\frac{1}{Q_L} = \begin{cases} \frac{R_l + R_s}{\omega_0 L} = \frac{R_L}{\omega_0 L} + \frac{R_s}{\omega_0 L} & \text{Series resonator} \\ \frac{\omega_0 L[R_l + R_s]}{R_s R_l} = \frac{\omega_0 L}{R_l} + \frac{\omega_0 L}{R_s} & \text{Parallel Resonator} \end{cases} \tag{2.4.3}$$

$$Q_e = \frac{\omega_0 L}{R_S} \text{ Series} \tag{2.4.4}$$

$$Q_e = \frac{R_S}{\omega_0 L} \text{ Parallel} \tag{2.4.5}$$

$$\frac{1}{Q_L} = \frac{1}{Q_u} + \frac{1}{Q_e} \tag{2.4.6}$$

The Q_e is defined as the external quality factor and Q_u is the unloaded resonator quality factor.

With eq. 2.4.4 and 2.4.5 the external Q can be defined and used to determine how it influences a resonator. The equations are derived from the simplified model of a resonator at/near resonance but the characteristics extracted from the equations can be applied to all forms of resonator models.

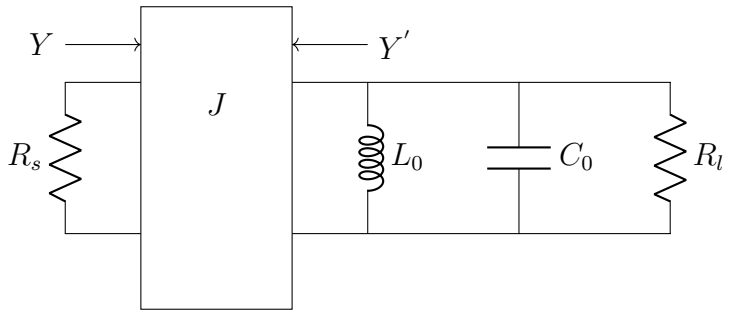

Figure 2.9: Scaling load to correct loaded quality factor

Using the parallel resonator as an example, the use of inverters allow for the scaling of loads to provide the required loaded quality factor as shown in Fig. 2.9.

$$Y' = \frac{J^2}{G_s} \tag{2.4.7}$$

$$Y = \frac{J^2}{G_l + j\omega C - 0 - j\frac{1}{\omega L_0}} \tag{2.4.8}$$

2.5 Coupling Coefficient

There are two forms of coupling, namely electrical coupling and magnetic coupling. Generally the coupling can also be named as negative and positive coupling due to the sign of the coupling coefficients when analyzing a filter numerically. In practical applications, coupling between two resonators consists of both coupling types, but if the layout of the filter is correct, a dominant

coupling mode can be established [4].

2.5.0.1 Electric Coupling

Electric coupling, or negative coupling, is a capacitive connection of two systems or structures by means of the interaction of their electric fields.

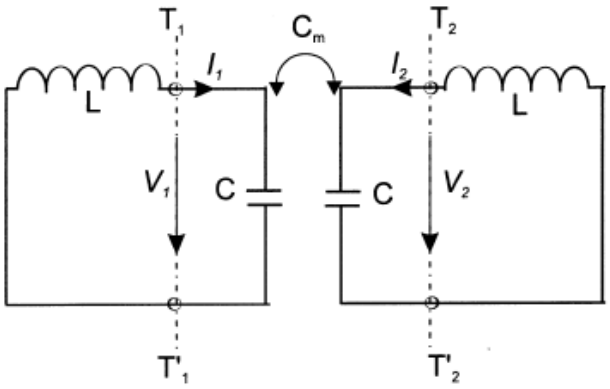

(a) Lumped LC resonator with mutual capacitance

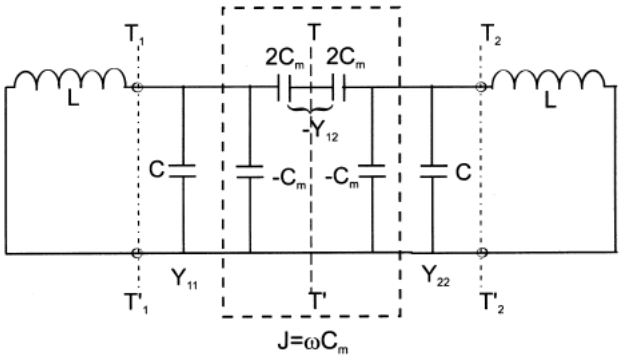

(b) Lumped LC resonator with expanded mutual capacitance circuit

Figure 2.10: Parallel LC resonator with mutual capacitance

Fig. 2.10(a) shows the mutual coupling element (C_m) as an invisible element that models the connection between the 2 LC resonators. Fig. 2.10(b) is an extended model of the same circuit as 2.10(a) and has the same characteristics. The coupling between the two resonators is easier to manipulate and to understand using the circuit in Fig. 2.10(b).

Applying a PEC or PMC wall at the T-T' junction results in a short or open circuit, respectively. The application of PEC and PMC shifts resonant frequency depending on the mode or wall that is applied. The frequency shift of the LC resonators can be expressed as eq. 2.5.1 or 2.5.2 when applying the PEC (f_e) or PMC (f_m) wall [4].

$$f_e = \frac{1}{2\pi\sqrt{L(C + C_m)}} \tag{2.5.1}$$

$$f_m = \frac{1}{2\pi\sqrt{L(C - C_m)}} \tag{2.5.2}$$

Using the frequencies achieved by applying the different walls, the electric coupling coefficient (K_E) can be derived eq. 2.5.3 [4].

$$k_E = \frac{f_m^2 - f_e^2}{f_m^2 + f_e^2} \tag{2.5.3}$$

2.5.0.2 Magnetic Coupling

Magnetic or positive coupling is the connection of two structures using the magnetic fields. This is represented in Fig. 2.11(a) as a mutual inductance of L_m [4]. Fig. 2.11(b) shows the extended model that can be used the same way as in Sec. 2.5.0.1.

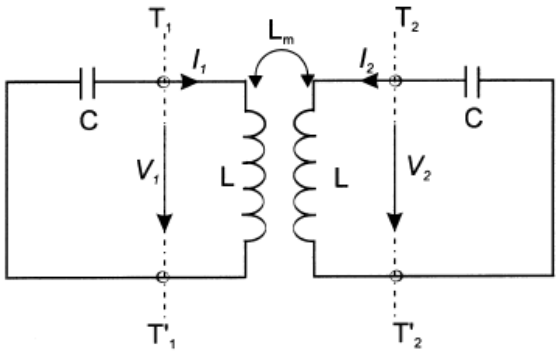

(a) Lumped LC resonator with mutual inductance [4]

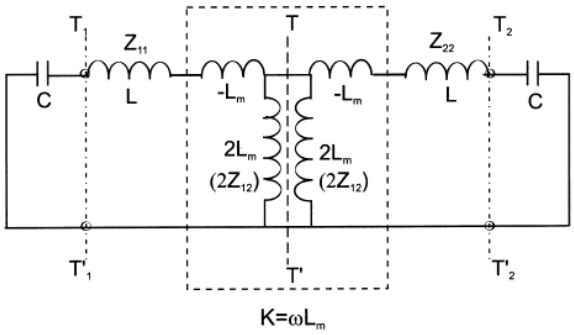

(b) Lumped LC resonator with expanded mutual inductance circuit [4]

Figure 2.11: Parallel LC resonator with mutual inductance

When applying the same methods of Sec. 2.5.0.1, the PEC and PMC walls affect the resonators in a similar way.

$$f_e = \frac{1}{2\pi\sqrt{(L - L_m)C}} \tag{2.5.4}$$

$$f_m = \frac{1}{2\pi\sqrt{(L + L_m)C}} \tag{2.5.5}$$

This leads to the magnetic coupling coefficient as expressed in eq. 2.5.6 [4].

$$k_M = \frac{f_e^2 - f_m^2}{f_m^2 + f_e^2} \tag{2.5.6}$$

The expansion shown in Fig. 2.10 and 2.11(b) shows that within the expanded circuit an inverters is observed. This implies inverters can be used to represent coupling in filter prototypes.

2.6 Coupled Resonator Filter

Coupled resonators allow for the use of a variety of filter topologies. This section explains the design of coupled resonator filter prototypes and typical implementation using interdigital and combline topologies.

2.6.1 Coupled Filter Prototype

The low-pass filter prototype shown in Fig. 2.2 and 2.3 consists of ideal elements with values derived from eq. 2.1.4 to 2.1.10 when using the Chebychev response. These elements are used to calculate the coupling factors and the optimal loaded Q factors [4].

$$k_{ij} = \frac{\Delta}{\sqrt{g_i g_j}} \tag{2.6.1}$$

$$q_S = \frac{g_0 g_1}{\Delta} \tag{2.6.2}$$

$$q_L = \frac{g_{n+1} g_n}{\Delta} \tag{2.6.3}$$

The term k_{ij} is the normalized coupling coefficient for a low-pass filter with the required fractional bandwidth (Δ). Eq. 2.6.2 and 2.6.3 are the normalized loaded q-factors of the resonator connected to the source and load [5].

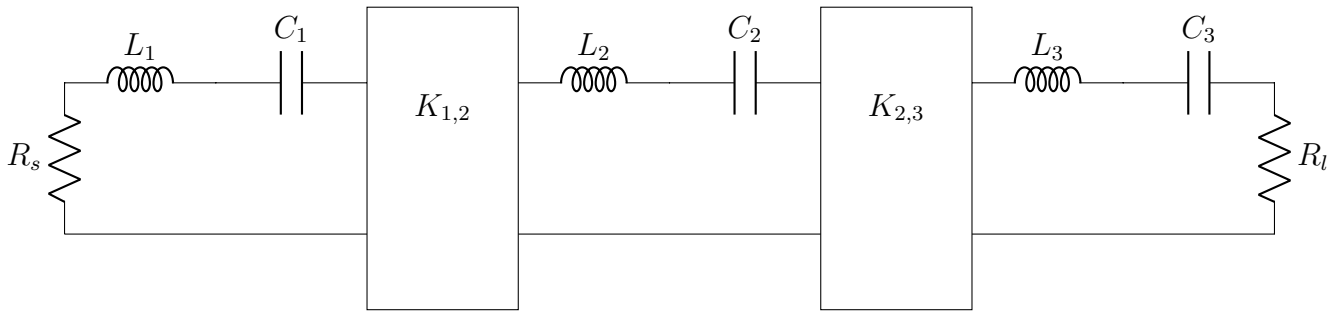

Figure 2.12: Series coupled resonator

$$K_{ij} = \sqrt{x_i x_j} k_{ij} = x k_{ij} \tag{2.6.4}$$

$$x = \frac{\omega_0}{2} \frac{\partial X}{\partial \omega}\Big|_{\omega=\omega_0} \tag{2.6.5}$$

$$R_S = \frac{x_1}{q_S} \tag{2.6.6}$$

$$R_L = \frac{x_n}{q_L} \tag{2.6.7}$$

The X is the reactance of the resonators of the resonators chosen for the filter. The reactance slope (x) at resonance (ω_0) shown in eq. 2.6.5 is used in addition to the coupling coefficient to derive the impedance inverter (K_{ij}) [4]. With the reactance slope the ideal load and source can be calculated. This method of designing in Eq.2.6.4-2.6.7 requires the assumption that all resonators are identical [5].

Similarly the filter model, where the resonators are chosen to be series resonators, can be modeled with shunt resonators with a known susceptance (B).

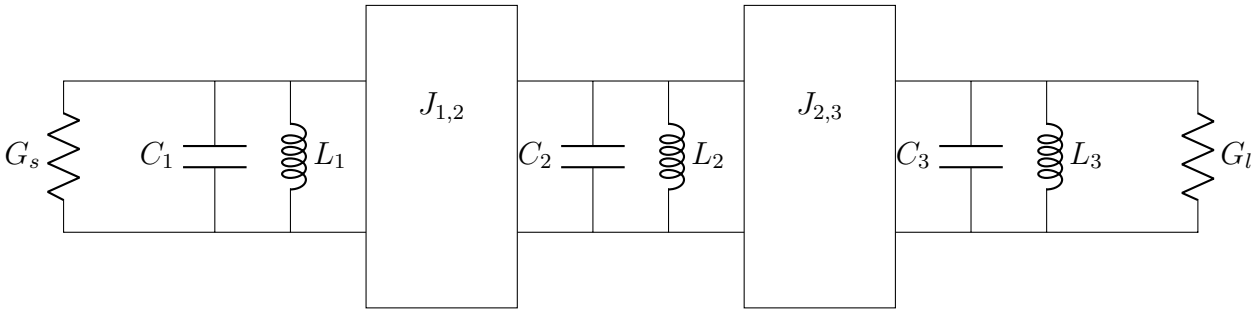

Figure 2.13: Parallel coupled resonator

$$J_{ij} = \sqrt{b_i b_j} k_{ij} \tag{2.6.8}$$

$$b = \frac{\omega_0}{2} \frac{\delta B}{\delta \omega}\Big|_{\omega=\omega_0} \tag{2.6.9}$$

$$G_S = \frac{b_1}{q_S} \tag{2.6.10}$$

$$G_L = \frac{b_n}{q_L} \tag{2.6.11}$$

The susceptance slope (b) at resonance is used to determine the admittance inverter (J_{ij}), source (G_S) and load (G_L). Using a LC resonator model eq. 2.6.5 and 2.6.9 is simplifies to:

$$x = \omega_0 L = \frac{1}{\omega_0 C} \tag{2.6.12}$$

$$b = \omega_0 C = \frac{1}{\omega_0 L} \tag{2.6.13}$$

2.6.2 Coupled Filter Topologies

Applying the theory from Sec. 2.6.1 on distributed circuits links mainly to the layout of the resonators and which parts of the resonator's field distribution couple between structures.
A common filter design choice for simplicity is to assume that the energy coupled to non-adjacent resonators are negligible, also known as cross coupling [7].

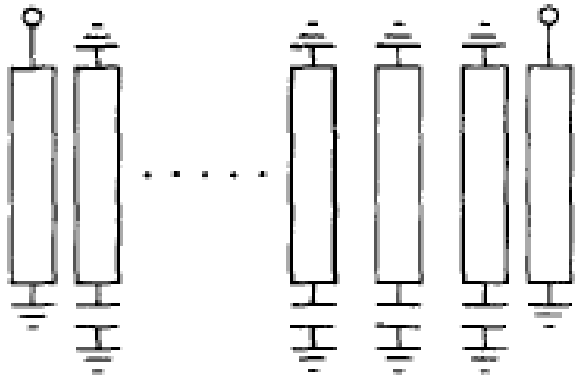

(a) Opposite side impedance transformation

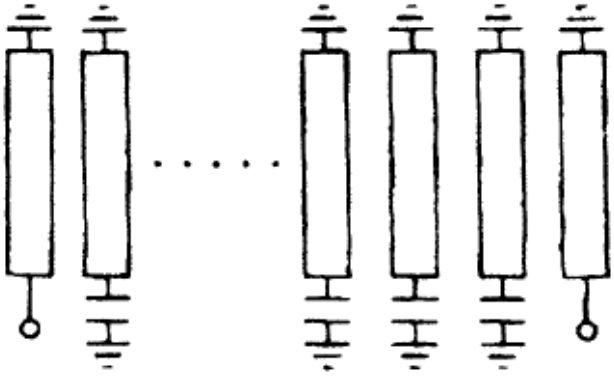

(b) Same side impedance transformation

Figure 2.14: Combline Filter

2.6.2.1 Combline

Combline is a common filter topology that is generally used in filters in the 10 GHz and lower range and provides a size reduction by loading the open ends of the resonators with capacitors. This reduces the required length of the resonators. The coupling between the resonators are broadside coupling and is dominated by magnetic coupling. The strongest electric coupling occurs at the loaded open end, where there is maximum electric field [14]. In the combline structure the maximum e-field is contained in a capacitive element and reduces the electric coupling between resonators [5].

Fig. 2.14 presents the typical layout of a combline filter where the resonators are connected using coupling [14]. The source and load is coupled into the filter and uses the coupling to transform and achieve the ideal loaded q-factor [14]. Fig. 2.14(a) and 2.14(b) show that there are two transformations when coupling into a filter namely, opposite side and same side transformation [14]. An alternative method is the use of a tapped-line input where the transformation of the input impedance is achieved with the use of a tapered line and the position on the first/last resonator [16, 17].

2.6.2.2 Interdigital

The interdigital filter consists of quarter wave length resonators, similar to that of a combline filter, and is also an inline filter where the basic topology has a negligible cross coupling. The interdigital filter is constructed with transmission lines that are broadside coupled, with the

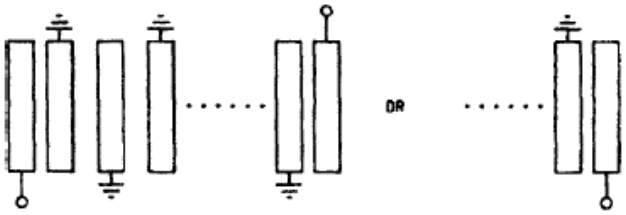

(a) Opposite side admittance transformation

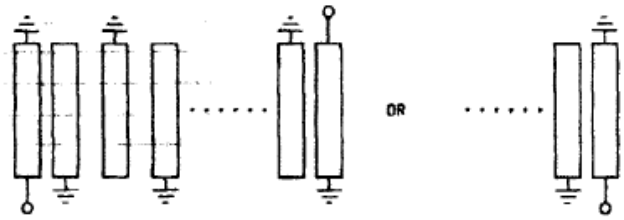

(b) Same side admittance transformation

Figure 2.15: Interdigital Filter

length of a quarter wavelength at the center frequency. The resonators are grounded at alternating sides as Fig. 2.15 shows. The alternating open/short circuit allows coupling with the electric and magnetic field, and results in a coupling that is stronger than in the combline filter. The magnetic coupling is weaker than the combline filter, but with the alternating grounds the electrical coupling improves the coupling between the resonators. An ideal interdigital filter consists of resonators with an electric length of 90°, but due to the fringe fields the total length of the resonators is reduced[5, 14, 18].

Looking at the input/output of an interdigital filter, shown in Fig. 2.15, a short or open circuit transformation can be used to provide the required loading.

2.7 Tunable Components

Much research has been done in order to reduce the size of the filter component of a system. For a multichannel system, such as most telecommunication networks, the ability to isolate a channel is important. Using multiple filters to achieve channel selectivity in a system, is spatially inefficient [19]. This project focuses on electrical tunable methods.

2.7.1 Micro-Electro-Mechanical Systems

Micro-Electro-Mechanical Systems (MEMS) use a potential difference to control a physical distance between two nodes. MEMS are used to create switches and adjustable capacitors [19]. The design in Fig. 2.16 shows a basic cantilever design that is used for both a switch and capacitor. The potential difference for the switch is applied between the cantilever and pull down electrode. This allows the cantilever to make contact with the switch contact point. The adjustable capacitor has a potential difference between the cantilever and ground. The capacitance is controlled by manipulating the height difference using the potential difference.

The advantage of using a MEMS capacitor is the extremely high Q, and for filter design the loss added to a resonator must be kept to a minimum. The difficulty of using MEMS capacitor

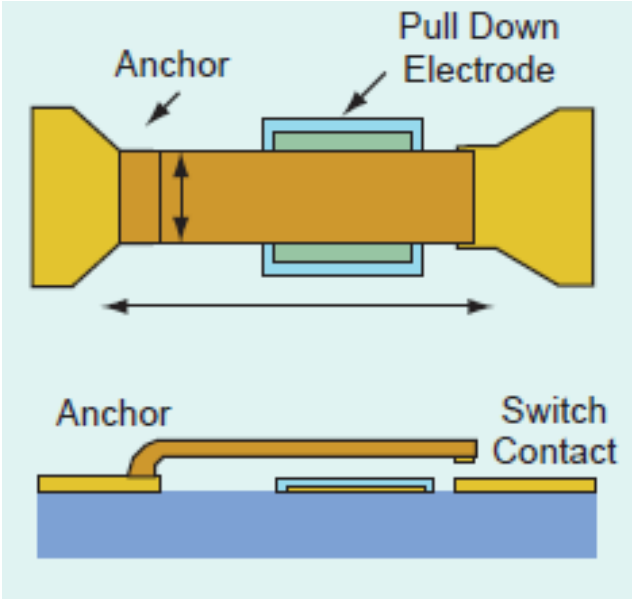

(a) Cantilever MEMS switch Design

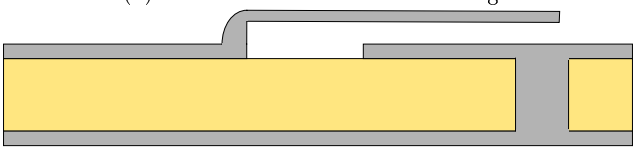

(b) Cantilever MEMS capacitor Design

Figure 2.16: Micro-Electro-Mechanical Systems

generally stems from its production. The cantilever must be thin so that when a potential difference is applied the cantilever will bend, but when the difference is reduced the MEMS will return to the original position. In order to implement MEMS it is best to integrate the component to a system. The reasoning behind the integrated implementation is to reduce the influence of MEMS packaging. The integrated implementation is difficult, but some aspects to also consider is the systematic weakening of the bending cantilever. Over time the MEMS will become more and more fragile and break [10].

2.7.2 Varactor Diode

The structure of the varactor diode is a P-N junction diode. When applying a reverse bias voltage a depletion region is created. The depletion region's size depends on the voltage applied over the nodes, which leads to a buildup of charged particles (holes and electrons) on either end of the depletion region. This is seen as a capacitor and the size of the depletion region determines the distance between the theoretical plates of the capacitor [6].

Fig. 2.17 shows that a good/theoretical diode does have an almost negligible current, but in reality the diode functions more like the weak/realistic diode represented in Fig. 2.17. Commercial varactors come in two types, abrupt and hyperabrupt, that differ in their capacitance range and a loss performance across the tuning range. There is a trade off between the tuning range and added loss. The choice depends on the application.

Varactors have an inverse relationship between the reverse voltage and capacitance. As the reverse voltage increases the depletion region, the capacitance becomes smaller [20]. The highest

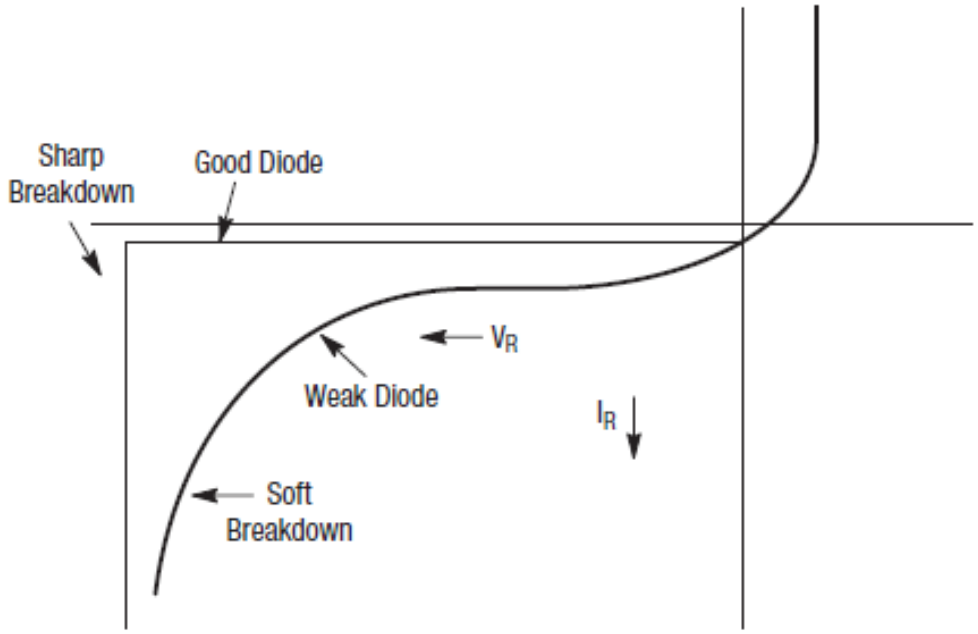

Figure 2.17: Ideal Diode vs Non Ideal Diode [6]

capacitance sensitivity occurs when the depletion region is the smallest. Fig. 2.18 shows the decay in sensitivity and shows that when the depletion region is large, any small change is a negligible when comparing to the total size of the region. When the depletion region is small any small change is not negligible when compared to the size of the region.

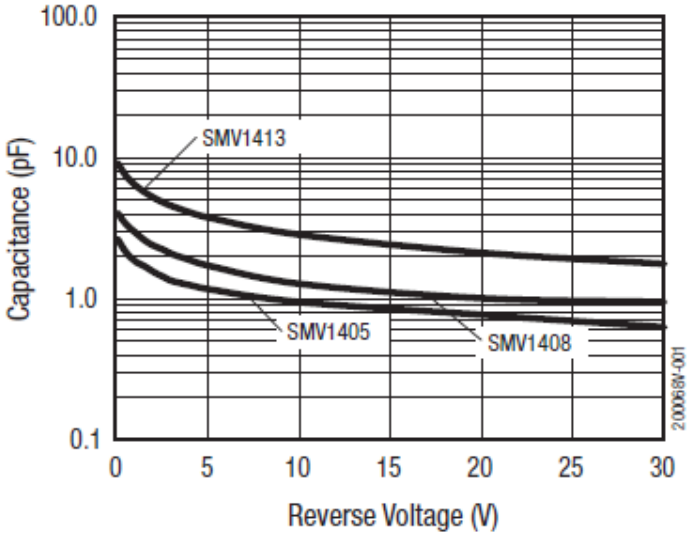

Figure 2.18: Capacitance vs Reverse Voltage

Fig. 2.18 shows the response of the SMV1405 to SMV1430 series from Skyworks. The abrupt junction is easier to model and has a known mathematical model. The hyperabrupt junction is less linear and curve fitting is used to show its typical behavior [6].

Abrupt varactors provide a method of tuning with lower loss, but does not provide the same tuning range as the hyperabrupt. This project needs to limit the loss added to the filter, thus

the design choice was made to use abrupt varactors [6].

2.8 Conclusion

For this project the Chebychev response is chosen for this filter, due to its focus on high isolation. Additionally the choice variable capacitance will be the varactor due to the availability.

Chapter 3

Prototype Filter Design

This chapter shows the design procedure, initial and complete simulation results of the tunable filter prototype. Sec.3.1 provides a study on the achievable frequency tunability for an ideal lumped element resonator and tunable capacitor combination. The coupling tunability for an ideal case is presented in Sec. 3.2. Section 3.3 presents the design and initial simulation results for the final filter topology, combining frequency and bandwidth tuning. The topology is tested in simulation for continuous tunability of a constant bandwidth. The simulated filter is prepared for manufacturing by the addition of biasing circuitry, shown in Sec. 3.4. The complete filter 3D model, including tuning components and biasing circuits, and simulation results are presented in Sec. 3.5.

3.1 Resonator Tunability

Implementing centre frequency tunability affects a resonator's electrical length and creates a new resonant frequency. This project utilizes a varactor diode as the tuning component due to the availability, cost, and ease of implementation. A varactor diode can be modelled as a lumped inductor, capacitor, and resistor in series [6]. While the inductor and resistor are due to packaging, bond wires and electron collisions, the capacitor value is controlled by the width of the depletion region. Since a varactor has a tunable depletion region, the most simplistic model of a varactor is a tunable capacitor. Therefore it is common practice to initially study the tunability of a filter topology by implementing ideal tunable lumped capacitors. Additional advantages of using capacitive tunable elements are that the fields are contained within the component and reduces the influence on adjacent structures.

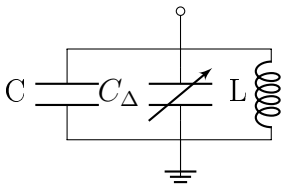

Figure 3.1: Parallel resonator with adjustable capacitor

The circuit shown in Fig. 3.1 represents a lossless lumped element resonator where the tunable components are simplified to an adjustable capacitor. Using eq. 3.1.1 and 3.1.2 an ideal lumped element resonator can be designed with a specific impedance and resonant frequency.

$$\omega_0 = \frac{1}{\sqrt{LC}} \tag{3.1.1}$$

$$Z_0 = \sqrt{\frac{L}{C}} \tag{3.1.2}$$

With some substitution, eq. 3.1.1 and 3.1.2 can be rearranged as shown in eq. 3.1.3 and 3.1.4.

$$C = \frac{1}{\omega_0 Z_0} \tag{3.1.3}$$

$$L = \frac{Z_0}{\omega_0} \tag{3.1.4}$$

When applying an adjustable capacitor, the resonator changes to the circuit in Fig. 3.1 and eq. 3.1.1 changes to:

$$\omega_0 = \frac{1}{\sqrt{L(C + C_\Delta)}} \tag{3.1.5}$$

This shows that any capacitance added (C_Δ) to the resonator lowers the resonant frequency.

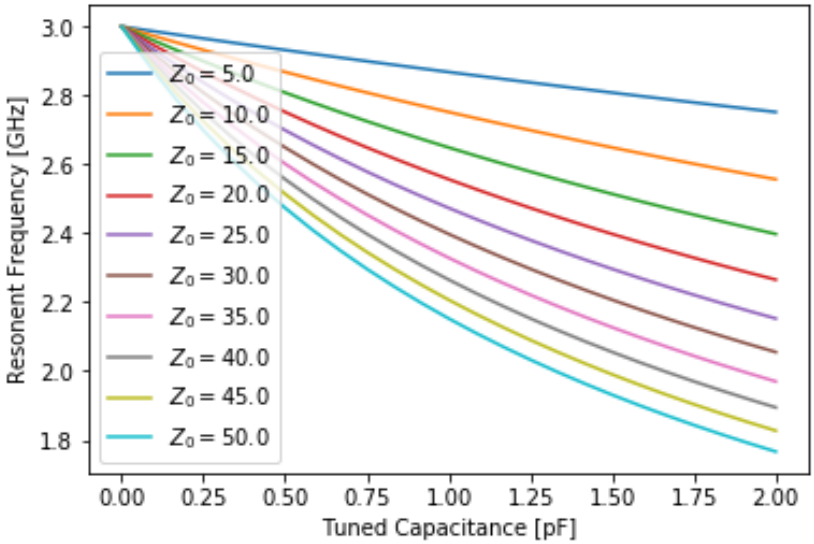

Figure 3.2: Ideal lumped element resonator capacitance sensitivity at different impedances

Fig. 3.2 shows that the sensitivity of a resonator increases as the impedance of the resonator is increased. This is because the added capacitance contributes more to the total capacitance as the resonator impedance increases.

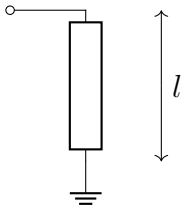

Figure 3.3: Transmission line resonator

Fig. 3.3 shows a transmission line resonator with the resonant frequency ω_0 and is known as a quarter wavelength resonator. Adding an adjustable capacitor (C) to this resonator changes the electrical length of the resonator.

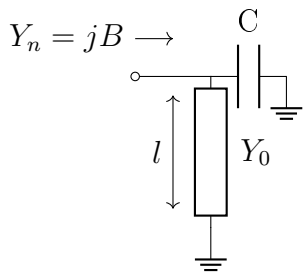

Figure 3.4: Transmission line resonator with adjustable capacitor

The resonator circuit in Fig. 3.4 uses a transmission line of length l, that is shorted on one side with an admittance of Y_0 in a medium, where c is the speed of light. For the ideal transmission line model the speed of light used is the speed of light in a vacuum. The circuit in Fig. 3.4 can be expressed as eq. 3.1.6

$$jB = j\omega C - jY_0 \cot \frac{\omega l}{c} \tag{3.1.6}$$

At resonance the susceptance equals to zero and by using software (Matlab or Python) the new resonance frequency can be determined.

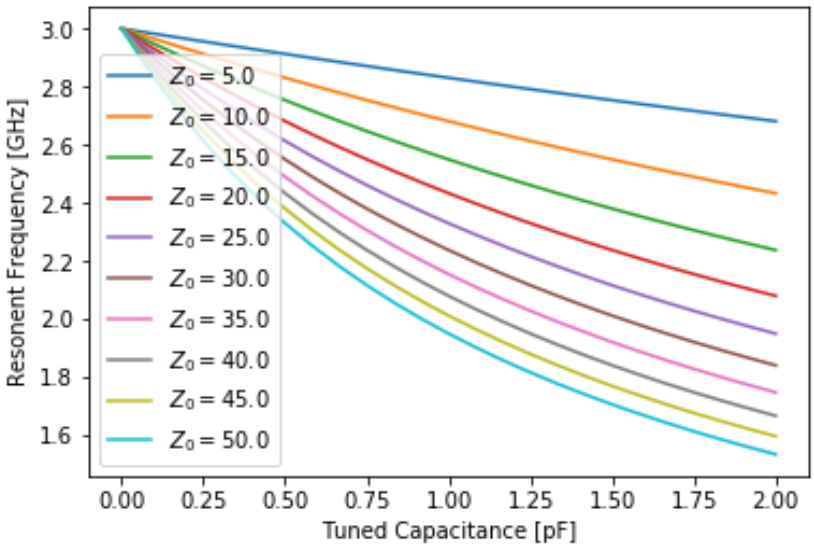

Figure 3.5: Transmission line resonator with adjustable capacitor

The slopes in Fig. 3.5 show that the tunability sensitivity of an ideal lumped element resonator and a lossless transmission line resonator have a similar sensitivity but to a different extent. For Z0 = 50 the tuned capacitance range causes a 1.6-3 GHz frequency shift in the TL resonator, and a 1.8-3 GHz range for the ideal lumped resonator model. This change is attributed to the difference in the slope parameter of a TL versus lumped resonator.

Adjustable components have a set range of value. This range can never obtain a value of zero and does not possess an upper limit of infinity. A resonator must be chosen to compensate for the limitations of the adjustable components. Depending on the tuning range required and the components available, the resonator must be chosen so that the sensitivity towards the added capacitance is correct.

This project uses an abrupt varactor from Skyworks, specifically the SMV 1405 abrubt varactor, which has the capacitance range of $0.63-2.67$ pF. Using eq. 3.1.6 and then applying the minimal capacitance allow for the solving of l when ω is set to $6\pi * 10^9$ rad/s. From this the frequency range of a resonator can be determined.

Table 3.1: Transmission line resonators sensitivity

Line Impedance	**Line Length**	**Minimum Frequency**	**Difference**
5	24.03 mm	2.684 GHz	315.5 MHz
10	23.10 mm	2.450 GHz	550.3 MHz
20	21.27 mm	2.142 GHz	858.4 MHz
50	16.46 mm	1.755 GHz	1.248 GHz
100	11.13 mm	1.426 GHz	1.574 GHz

Table 3.1 shows that the length of the resonator must be adjusted to allow an upper frequency limit of 3 GHz. Making a resonator too sensitive can and has caused production issues when adding the coupling structure, which adds more capacitance to the resonator.

3.2 Coupling Tunability

The coupling is an important component to be able to adjust when creating a tunable filter with a fixed bandwidth. The coupling is directly proportional to the fractional bandwidth, which means to sustain an absolute bandwidth from a higher to a lower center frequency, the filter needs the coupling coefficient to increase as the fractional bandwidth increases.

The filter design shown in Fig. 3.6(a) uses the varactor structure to limit the growth of the coupling between resonators, meaning that [2] uses varactor to regulate the growth of coupling strength where [1] uses the Non-resonant node to directly control the coupling strength of the filters design shown in Fig. 3.6(b).

With some alteration to the design shown in Fig. 3.6(a), the coupling strength can have a direct relationship with the varactor capacitance value. This means that the coupling strength range will be dependent on the varactor capacitance range.

The model was designed under ideal conditions where there are no loss, zero coupling between the resonators and no inductance added due to bonding wires. Under these assumption the varactor can be modeled as a capacitor (C) as shown in Fig. 3.7. To ensure the bridge acts as an inverter, theoretical capacitors are added to the structure. The capacitors will be used to model the varactor structure's influence on the resonator.

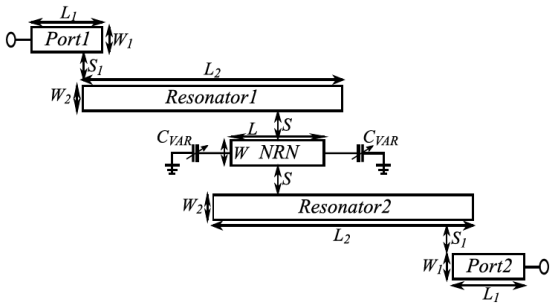

(a) Coupling tuning using Non-resonant node inverter shown in Fig. 1.1

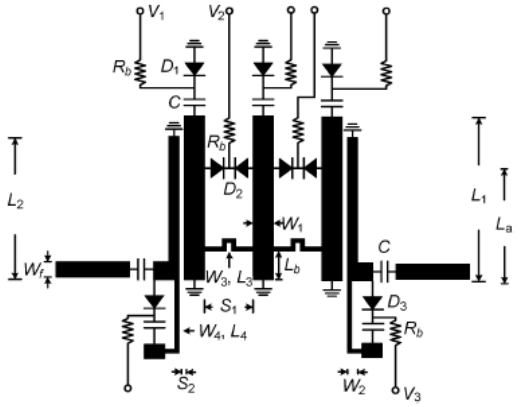

(b) Coupling structure used by [2] shown in Fig. 1.4

Figure 3.6: Filter designs examples with coupling control

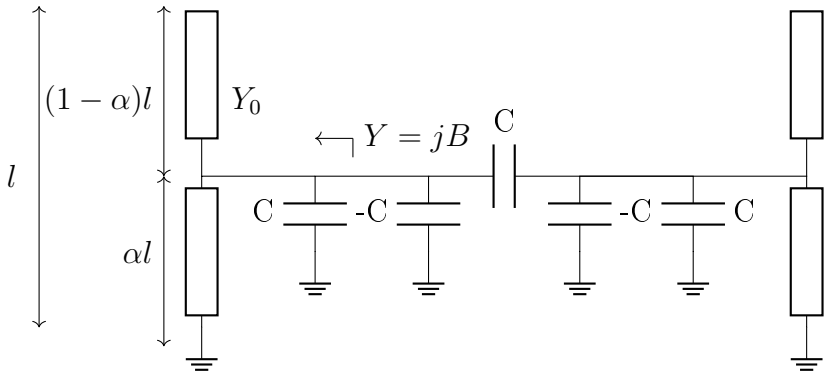

Figure 3.7: Diode structure to realise an inverter

The susceptance of the resonator can be defined as

$$jB = jY_0 tan(\frac{\omega l(1-\alpha)}{c}) + j\omega C - jY_0 cot(\frac{\omega l \alpha}{c}) \tag{3.2.1}$$

The term α is used to indicate the position on the resonator to which the varactor bridge connects, as shown in Fig. 3.7. The closer the varactor bridge is to the short circuited side of the resonator, the lower the value of α is. The value of α only exist between 0 and 1. The new susceptance determined by eq. 3.2.1 shows similar sensitivity to capacitance as that of the resonator in Fig. 3.4, when comparing resonator frequency.

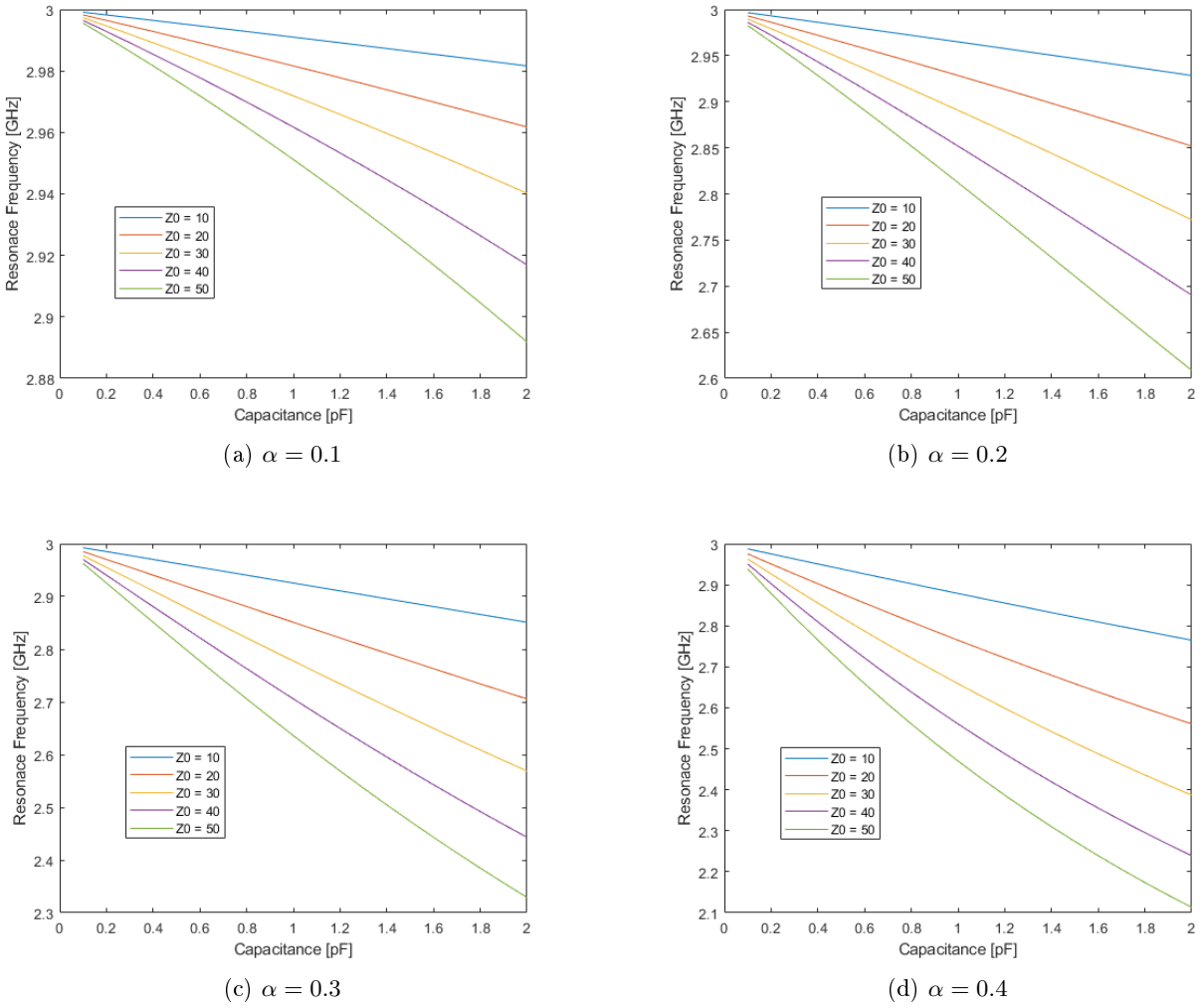

(a) $\alpha = 0.1$ (b) $\alpha = 0.2$

(c) $\alpha = 0.3$ (d) $\alpha = 0.4$

Figure 3.8: Frequency shift of an ideal resonator for different tapping positions α of a varactor bridge and various line impedances.

A simulation-based investigation of the tapping position's influence on the tunability of the resonator is done. The results shown in Fig. 3.8 indicate that as the value of alpha is increased the range the resonant frequency shifts increases and this is true for all resonator impedance options tested. It can be said that the resonators' capacitance sensitivity is directly proportional to the value of α.

Furthermore, the required tapping position of the varactor bridge, for specific resonance frequency when considering a fixed capacitance value and line impedance is investigated. The results shown in Fig. 3.9 indicates that the placement of the coupling structure shifts the resonant frequency if the resonator length is not adjusted.

Factors that influence coupling coefficient are shown in $J_{ij} = \sqrt{b_i b_j} k_{ij}$. In this case the characteristic admittance of the inverter and the susceptance slope is both dependent on the value of C. The downwards shift of the resonant frequency has to be compensated with large enough increase of the varactor bridge's capacitance. By looking at Fig. 3.9 all the graphs show that the value of α influences the resonant frequency, but this can be compensated by changing the line impedance.

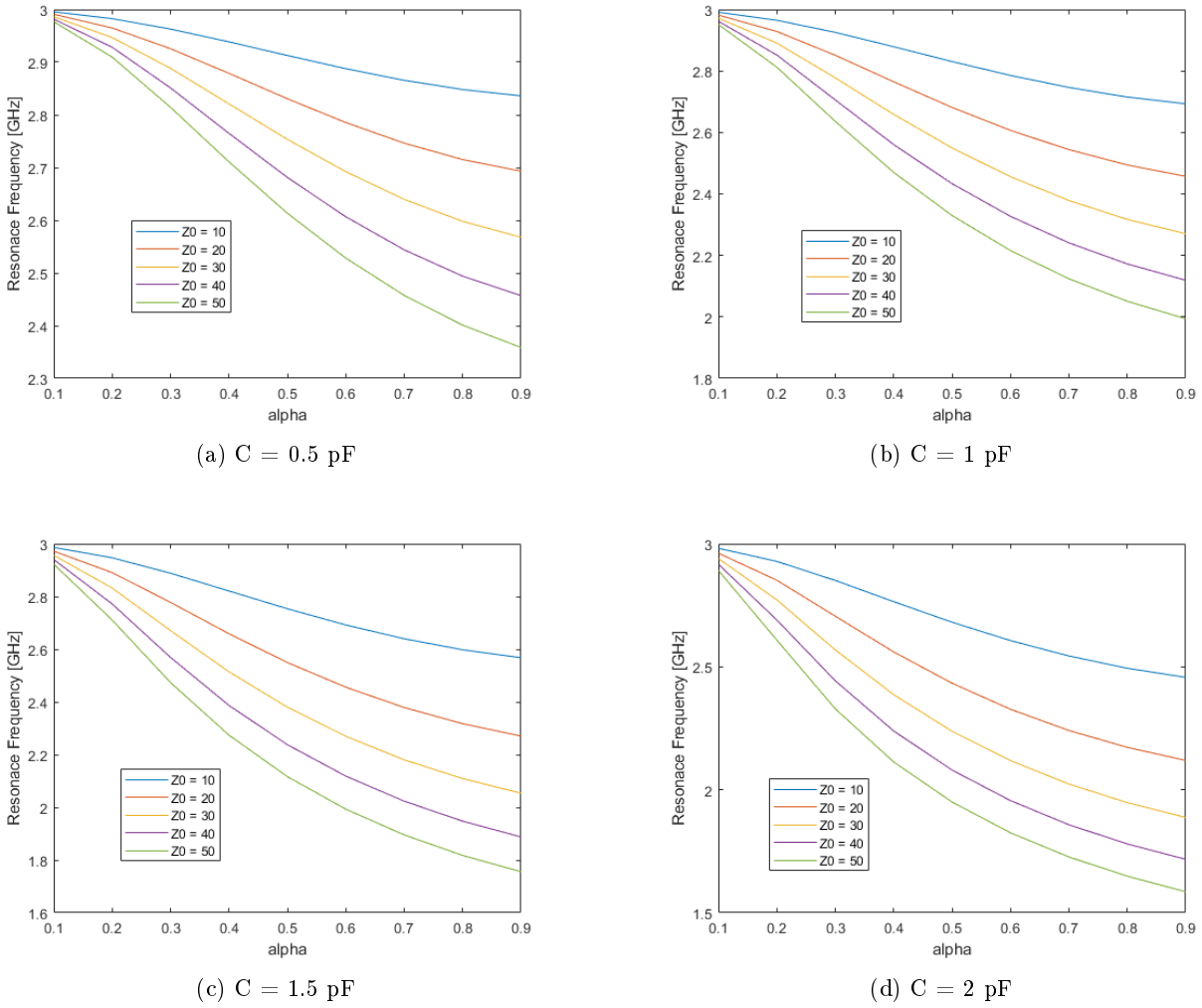

(a) C = 0.5 pF

(b) C = 1 pF

(c) C = 1.5 pF

(d) C = 2 pF

Figure 3.9: A resonator's resonant frequency different line impedance and α values

To determine the effect of the varactor structure tapping point and capacitance on the coupling strength, a simulation is performed for various line impedances. The different coupling coefficients in Fig. 3.10 show that the coupling strength increases as the value of α increases. As shown in Fig. 3.9, higher α values make the resonator more sensitive to added capacitance. The coupling coefficients shown in Fig. 3.10 are determined at the corresponding resonant frequency shown in Fig. 3.2.

3.3 Application of Primarily Electrical Adjustable Coupling and Frequency Tunability

The previous two sections looked at how the resonator was affected by the added capacitance and a varactor structure at various tapping positions. As mentioned in Sec. 3.1, the components available in reality do not have a minimum capacitance of zero and that certain design choices must be made to obtain the desired results. It was shown in Sec. 3.2 that the addition of any capacitance value to the varactor bridge shifts the resonant frequency and the intensity of the shift depends on both the line impedance and the placement of the varactor bridge.

This project requires frequency tunablity to accurately control the frequency shift of the filter.

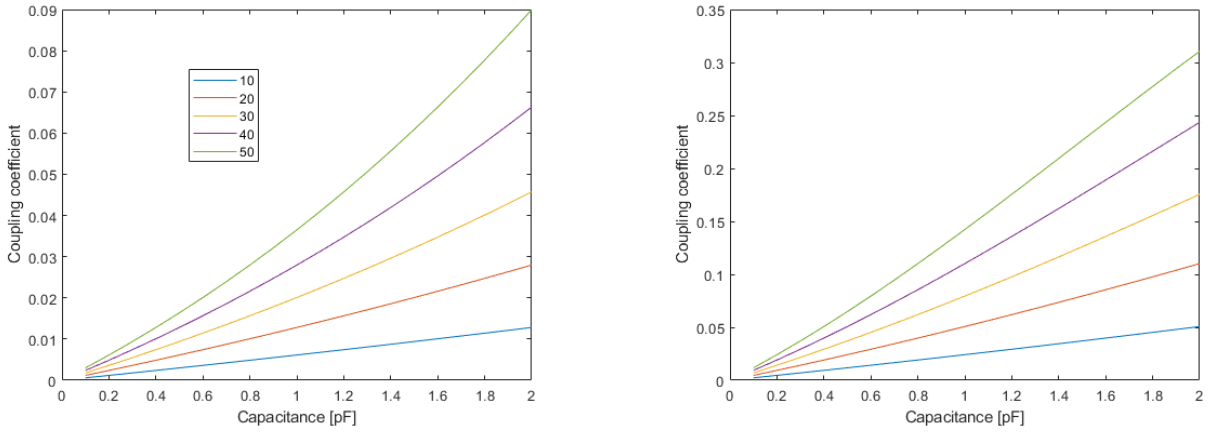

(a) $\alpha = 0.1$

(b) $\alpha = 0.2$

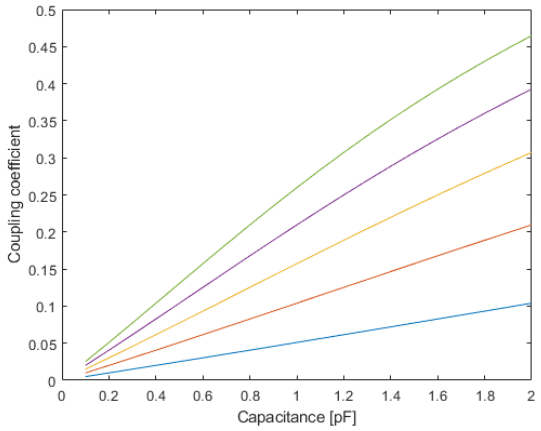

(c) $\alpha = 0.3$

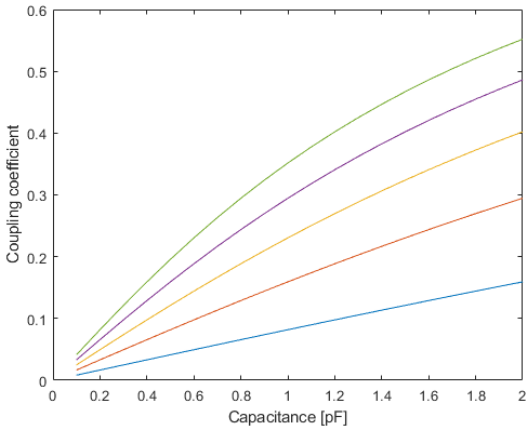

(d) $\alpha = 0.4$

Figure 3.10: Coupling sensitivity at different impedance and different α values

The use of the varactor structure has been shown to shift the resonant frequency, but with no control over the extent of the shift. In order to provide control, an additional tuning component is required.

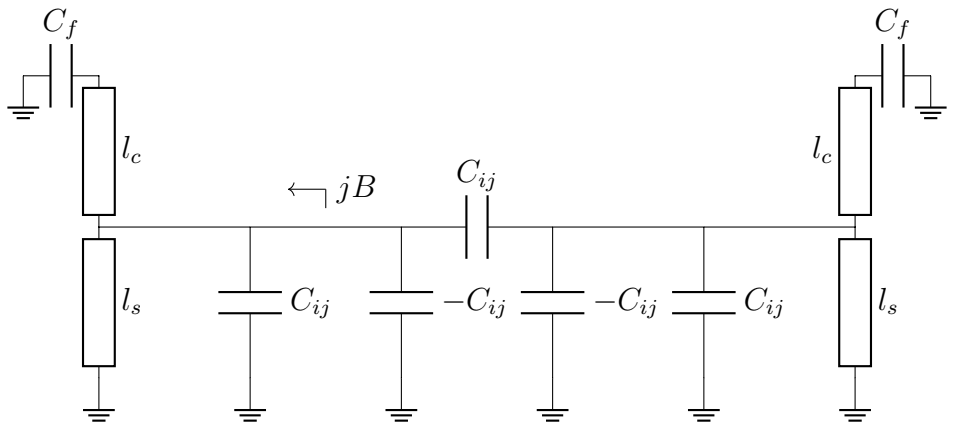

Figure 3.11: Ideal transmission line resonator model

Fig. 3.11 shows the addition of a frequency tuning capacitor (Cf) to each transmission line

resonator's open end. The new susceptance slope parameter of the resonator becomes

$$jB = j\omega C_{ij} + Y_0 \frac{Z_0 + \frac{tan(\frac{\omega l_c}{c})}{\omega C_f}}{\frac{1}{j\omega C_f} + jZ_0 tan(\frac{\omega l_c}{c})} - jY_0 cot(\frac{\omega l_s}{c}) \tag{3.3.1}$$

The susceptance eq. 3.3.1 shows that the varactor structure is represented by the capacitor C_{ij} and the capacitor in control of the frequency is shown as C_f. The varactor structure capacitance range is 0.32-1.34 pF, per the data sheet of the chosen component. To scale the capacitance of the varactor, represented by C_f, two series connected capacitors are added where one is the varactor and the other capacitor is a fixed capacitor that is substantially larger. In the case of this project the fixed capacitor is chosen as 10 pF and this means that using the SMV 1405 the ideal C_f is 0.59 to 2 pF.

To allow for some adjustments to the bandwidth, the capacitance of all the components will not be set to the minimum or the maximum, but rather to a off-centered value in the direction of the minimum tunning range. Setting the varactor to a capacitance value to the lower end preserves as much of the sensitivity as possible.

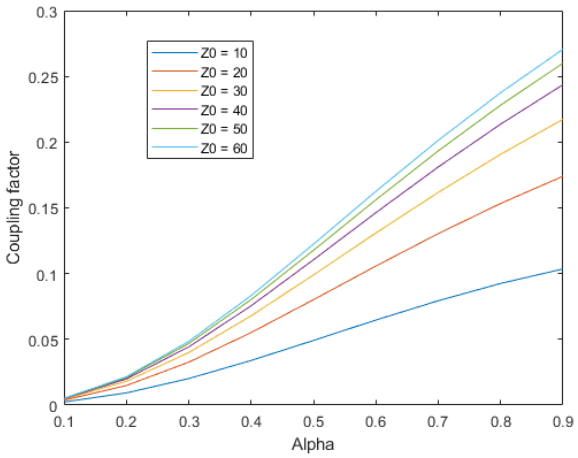

Figure 3.12: Coupling factor with $C_f = 1pF$ and $C_{ij} = 0.5pF$ with different line impedances resonating at 3.05 GHz

An additional study was done to determine the influence the transmission line impedance has on the coupling factor range by keeping all capacitance values fixed and changing the alpha values the transmission line length is used to maintain a constant resonant frequency. Fig. 3.12 shows the coupling sensitivity towards the transmission line impedance increases as the impedance is increased. This can lead to design choices using higher impedance transmission lines to increase to potential range of the filter and compensates for the limited range of tunable components.

3.3.1 Adaptation to Varactor Structure

The filter shown in Fig. 3.6(a), shows the addition of transmission line (L_3) used to increase the positive coupling. Using the SMV-1405 in the SC-079 packaging provides a longer package than the SOD-882 packaging, but the addition of transmission lines to the varactor structure ensures that the space between resonators is great enough to be considered decoupled.

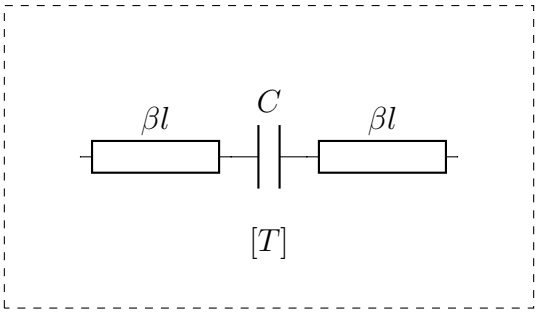

Figure 3.13: Varactor bridge modified to decouple resonators

An ABCD matrix is used to model this sub-circuit in order to ensure that the bridge can still be seen as an inverter. The matrix is shown in eq. 3.3.2. This is assuming that at the frequencies the filter is working, $\sin(\beta l)$ extremely small.

$$[T] = \begin{bmatrix} Cos(\beta l) & jZ_0 Sin(\beta l) \\ jY_0 Sin(\beta l) & Cos(\beta l) \end{bmatrix} \begin{bmatrix} 1 & \frac{1}{j\omega C_{ij}} \\ 0 & 1 \end{bmatrix} \begin{bmatrix} Cos(\beta l) & jZ_0 Sin(\beta l) \\ jY_0 Sin(\beta l) & Cos(\beta l) \end{bmatrix} = \begin{bmatrix} 1 & \frac{1}{j\omega C_{ij}} \\ 0 & 1 \end{bmatrix} \tag{3.3.2}$$

To establish how much transmission line is needed to decoupled the resonators magnetically. A CST simulation was used to determine how sensitive the relationship between coupling strength and coupling distance. A eigon mode solver was used and PMC and PEC wall was placed between the resonators so that f_e and f_m can be determined. Using these values the magnetic coupling strength can be determined by using Eqn. 2.5.6.

The results shown in Fig. 3.14 indicates that the magnetic coupling strength does taper off quickly.

3.3.2 AWR Implementation

For this project the available dielectric is Rogers RO 4003C ($\epsilon_r = 3.55$). Initially the filter was designed using the 0.203 mm thick dielectric, but due to manufacturing difficulties where the machine removed too much material. The dielectric thickness was changed to the 0.508 mm of the same dielectric type.

The filter used to test this coupling structure will be designed to provide a initial bandwidth of 300 MHz at the center frequency 3.0463 GHz ($f_1 = 2.9$ GHz and $f_2 = 3.2$ GHz). With the model done thus far it was shown that using a high impedance transmission line increases the sensitivity towards additional capacitance added to a transmission line filter. Additionally for a higher impedance transmission line, α achieves a high coupling factor whilst reducing the sensitivity between the line impedance and the coupling factor. With a lower α value the influence the coupling structure has on the resonant frequency is reduced, thus counteracts the increases in sensitivity towards added capacitance.

For this project the filter is designed for a tunability of 1 GHz. The capacitance value of C_{ij} and C_f are 0.5 pF and 0.9 pF respectively. Fig. 3.12 shows obtaining a coupling coefficient of approximately 0.1 can be achieved on a 60 Ω transmission line with an alpha between 0.4 and 0.5.

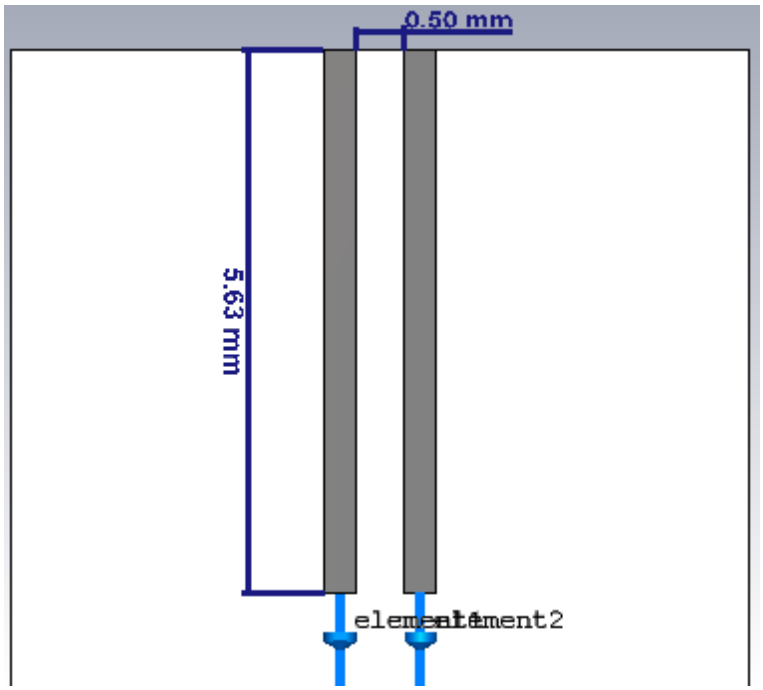

(a) CST Simulation

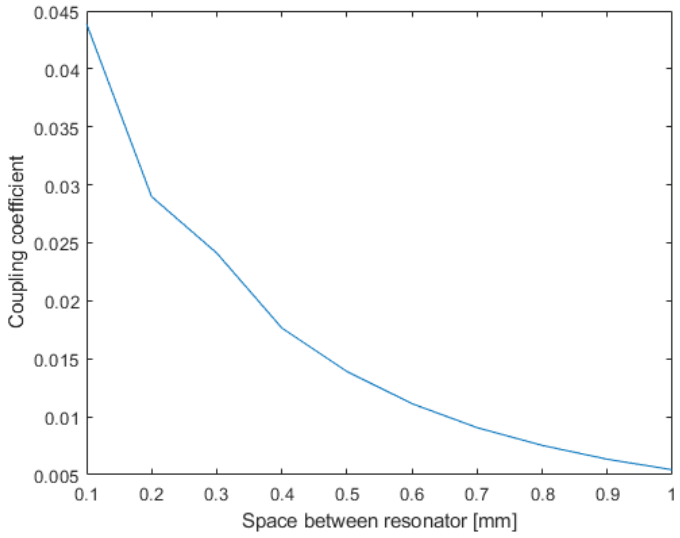

(b) Coupling strength

Figure 3.14: 60 Ω Quarter wavelength resonator CST coupling with a $C_f = 0.9$ pF

Fig. 3.15 shows a third order lumped element bandpass filter model and response, with a bandwidth of 300 MHz at the center frequency 3.0463 GHz ($f_1 = 2.9$ GHz and $f_2 = 3.2$ GHz). The low pass prototype used a maximum pass-band insertion loss of $IL_{pb} = 0.001$ dB. This ideal filter will be implemented using the coupling structure.

The source and load transformation are made with the use of a tapered line. Using the group delay of the ideal lumped element filter shown in Fig. 3.15, the one port group delay is used to indicate the time delay of the reflect energy at different frequencies. The group delay can be used to make the necessary adjustments to the resonator length and input tap placement when measuring the group delay of the input tap and the first resonator. With the second resonator

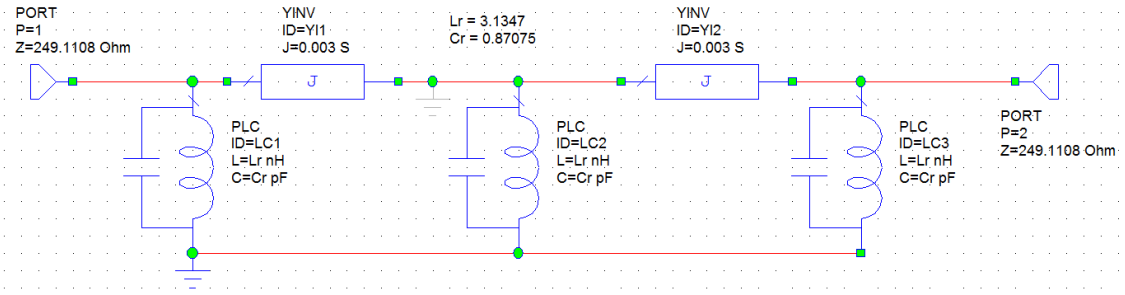

(a)

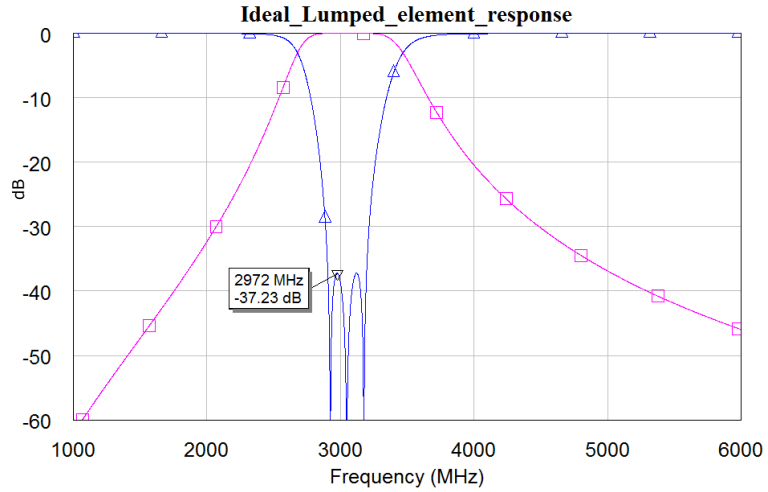

(b)

Figure 3.15: Lumped element ideal coupled filter

the coupling structure placement determines the inter-resonator coupling and establish the accuracy of the coupling structure model used so far.

When focusing on the pass-band, as shown in Fig. 3.16, using the varactor coupling structure, the group delay can be recreated with reasonable accuracy. For this model the influence of the coupling structure is tested.

The line shown in both Fig. 3.17(a) and 3.17(b) labeled as "Microstip ideal model alternative Bridge placement" is provided with a smaller alpha value to determine the influence on the group delay. When expanding the range of the simulation, an additional group delay peak is shown in Fig. 3.17(a). Fig. 3.17(a) shows that the peak generated by the coupling structure is sensitive towards the placement of the coupling structure. Fig. 3.17(b) shows that smaller alpha values reduces the resonator sensitivity towards the capacitance the coupling structure adds. This is proven by the upward shift of the group delay peaks in the pass-band.This means that some sensitivities shown in the earlier testing are still correct and that when designing the coupling structure the generated group delay peak must be taken into account. Additionally this model simulation also disproved the initial assumption that the transmission lines added to the coupling structure does not influence the filter response.

The generation of a group delay peak indicates that when modeling the filter using ideal transmission lines, the model must take into account any lines added to reduce the magnetic coupling. This expands the model from the circuit shown in Fig. 3.11 to the circuit model shown in Fig.

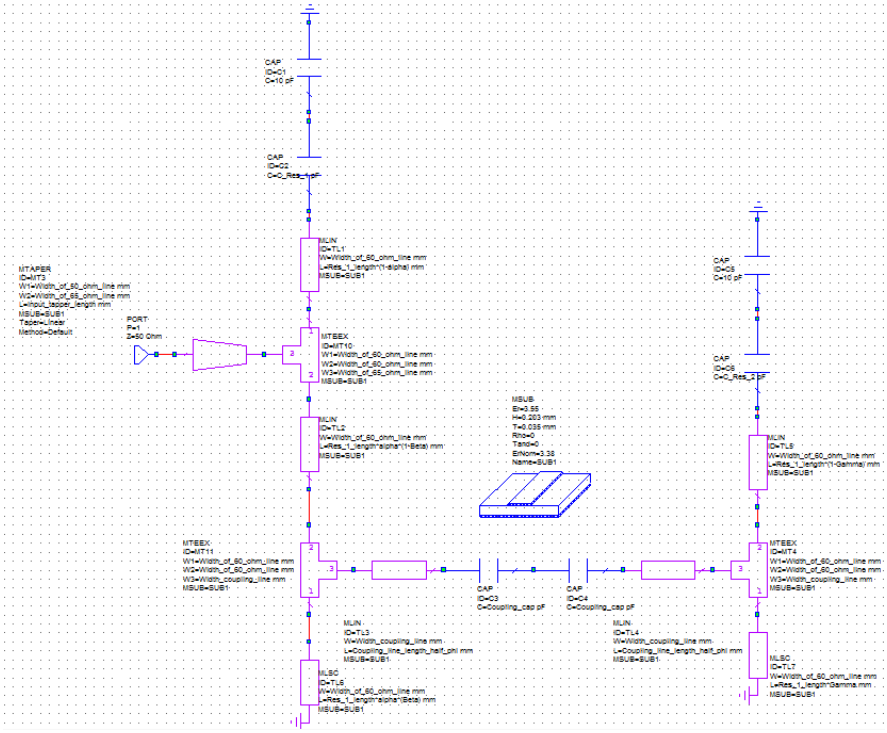

(a) Ideal Microstrip model of 2 resonators filter

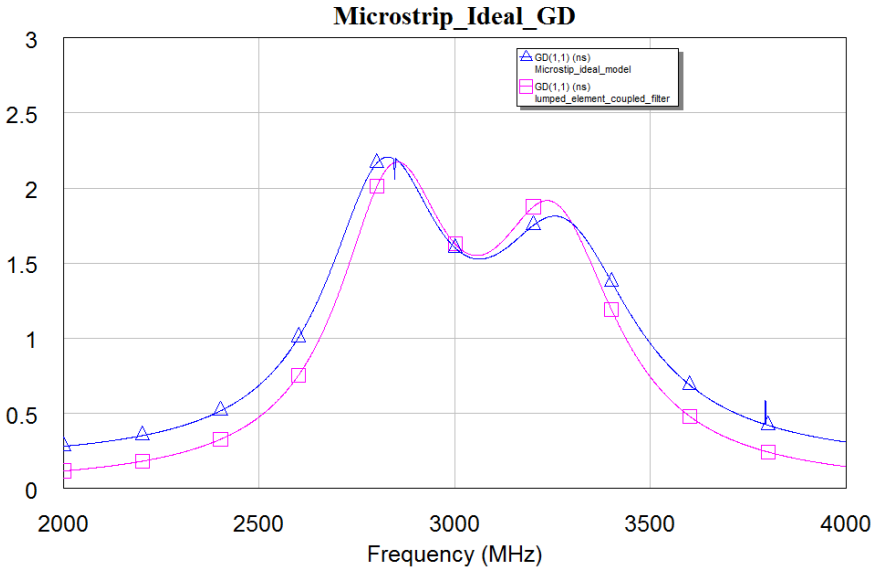

(b) Ideal lumped element and Ideal Microstip Group delay

Figure 3.16: Group delay comparison

3.18.

The line impedance and length added to the coupling structure is named Z_{ij} and l_{ij}. Shown in eq. 3.3.4 the added transmission line transforms the jB.

$$jB = jY_0 \frac{Z_0 + \frac{tan(\frac{\omega l_c}{c})}{\omega C_f}}{\frac{1}{\omega C_f} - Z_0 tan(\frac{\omega l_c}{c})} - jY_0 cot(\frac{\omega l_s}{c}) \tag{3.3.3}$$

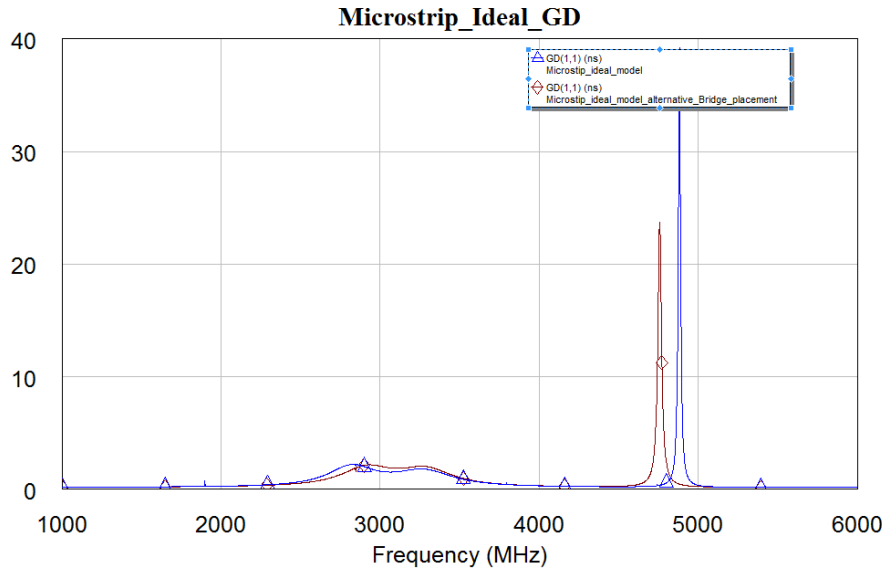

(a)

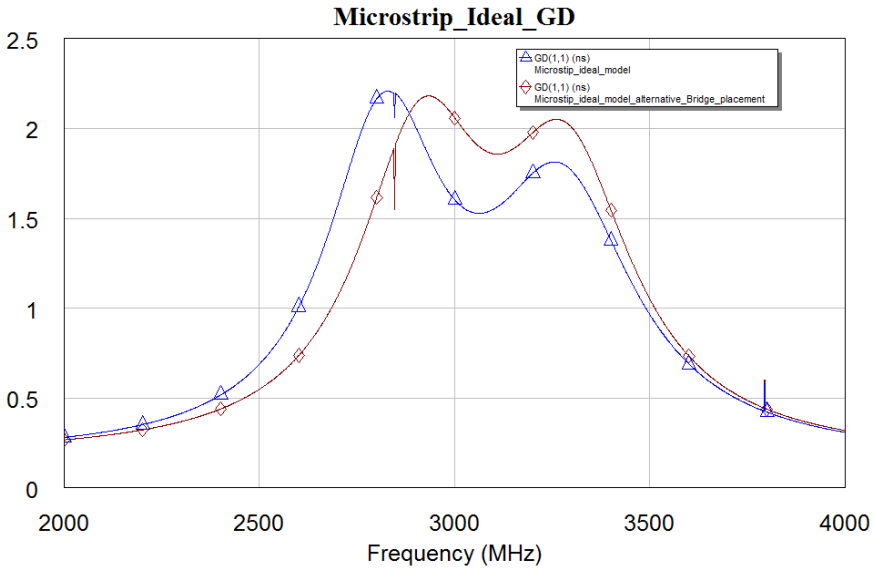

(b)

Figure 3.17: Group delay response for alternative coupling structure placements

$$jB' = jY_{ij}\frac{Z_{ij} + \frac{tan(\frac{\omega l_{ij}}{c})}{B}}{\frac{1}{B} - Z_{ij}tan(\frac{\omega l_{ij}}{c})} + j\omega C_{ij} \tag{3.3.4}$$

Using the new model for the resonator the influence on the coupling is shown in Fig. 3.20(a). Comparing to the previous results in Fig. 3.12 the resonator line is changed to maintain a constant 3.0463 GHz resonant frequency. The addition of transmission line l_{ij} shows that the coupling strength increases significantly. In Fig. 3.12 the 60 Ω transmission line resonator reached a maximum coupling factor of 0.26. The new model shows that the required coupling coefficient can be reach with a alpha value between 0.4 and 0.3 depending on the length of l_{ij}. Additionally the length of l_{ij} also determines the influence C_{ij} has on the resonant frequency, as shown in Fig. 3.19 a longer l_{ij} increases the range the resonant frequency shifts. This

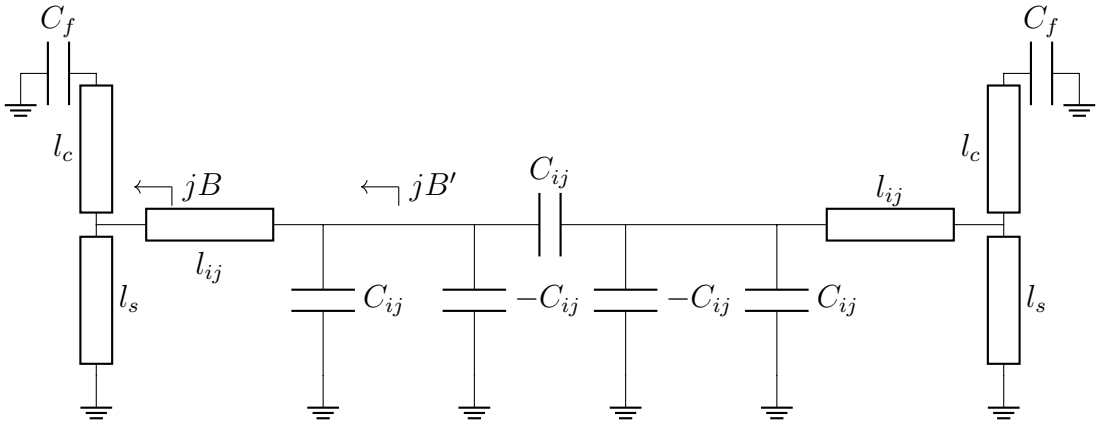

Figure 3.18: Ideal transmission line resonator taking into account magnetic coupling reduction transmission lines

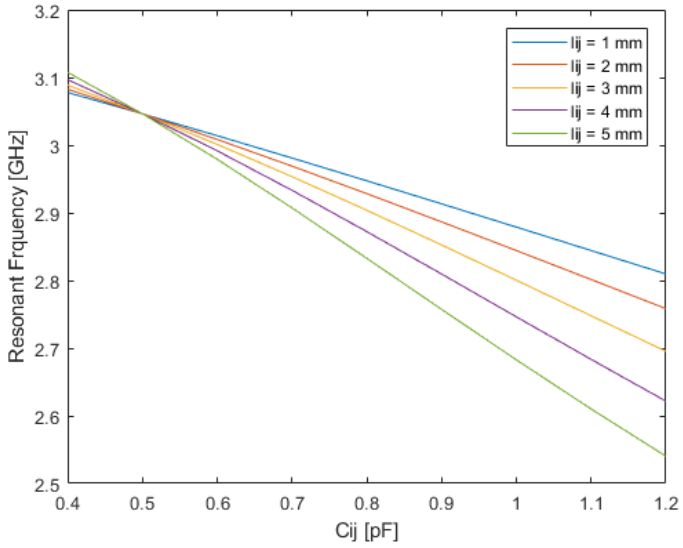

Figure 3.19: The influence C_{ij} has on a 60 Ω transmission line resonator with an $\alpha = 0.4$.

leads to the realisation that using a transmission line l_{ij} is the same as using a larger varactor capacitance.

The results shown in Fig. 3.20(b) indicate that the end resonator loaded Q factor (q_s) decreases as α increases. The low qs value indicates that the source and load is coupled to the end resonator really strong meaning that coupling into the resonator is unrealistic due to a very small coupling gap between the input/output and a physical connection is a realistic solution.

The influence of l_{ij} is now known, but the influence of the coupling structure's line impedance (Z_{ij}) must be determined. Fig. 3.21 shows the results of testing the ideal transmission line model by setting the line length l_{ij} constant and changing the line impedance of that same line. The resonator length is changed to maintain a constant resonant frequency at 3.0463 GHz. The results in Fig. 3.20(a) and 3.20(b) show that the solver at α=0.1 finds a solution other than what is expected when following the trend of the data , which requires more research to find a optimal solver but is outside the scope of this project.

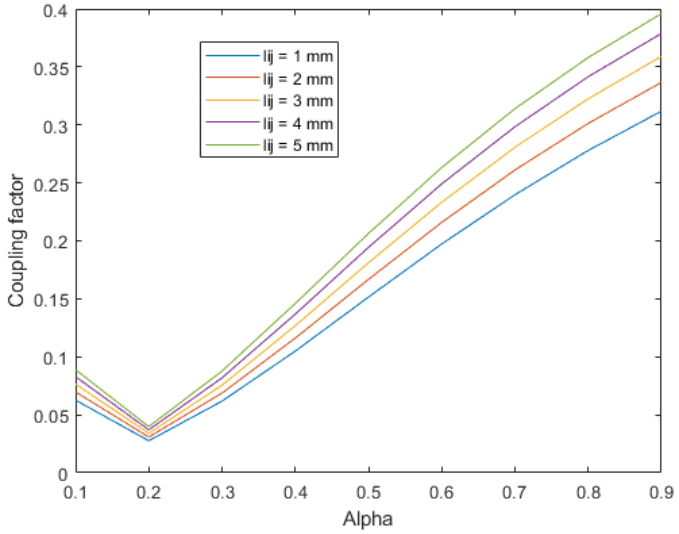

(a) Testing the coupling strength with different l_{ij} and α values on a 60 Ω transmission line at 3.0463 GHz

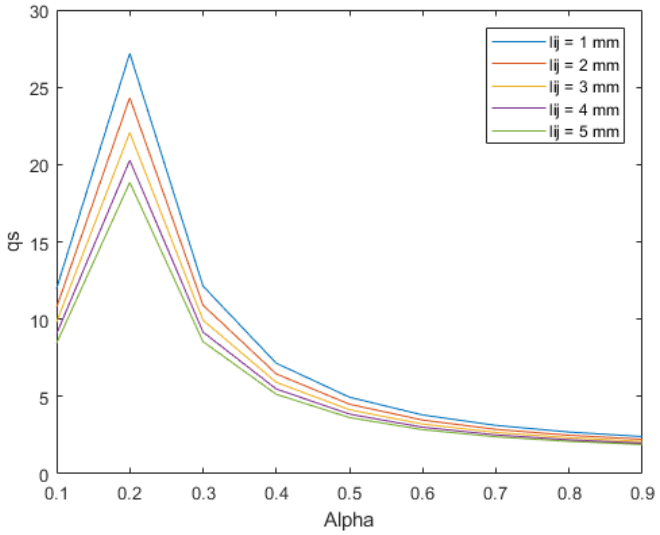

(b) Loaded Qs values for the coupling factor values shown in Fig. 3.20(a)

Figure 3.20: Modeling the influence of the added transmission line to the resonator model where $Z_{ij} = 100\ \Omega$, $C_f = 0.9$ pF and $C_{ij} = 0.5$ pF

Testing the model showed that the line impedance of l_{ij} has a smaller influence on the coupling strength and quality factors as shown in Fig. 3.21. The results show that the line impedance can be used to increase the coupling strength and this also decreases q_s values.

Using the knowledge gained of the system from the simplified models, the 3rd order filter shown in Fig. 3.15 was implemented. The pass-band can be recreated with reasonable accuracy and the results show clearly the influence the coupling structure has on the filter response.

The model shown in Fig. 3.22 assumes ideal conditions (no loss and ignoring any influence of the component packaging) and no biasing circuits are implemented on this model. To determine the tunablity of the filter an RLC model for the varactors is used to represent the loss the varactor

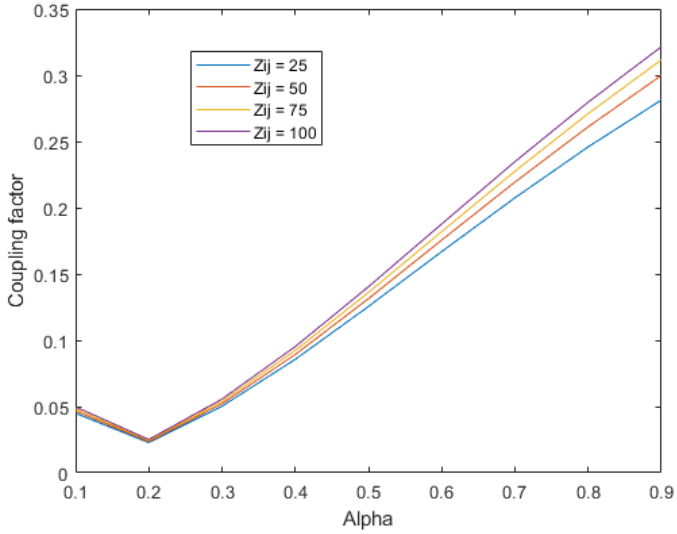

(a) Testing the coupling strength with different Z_{ij} and α values on a 60 Ω transmission line at 3.0463 GHz

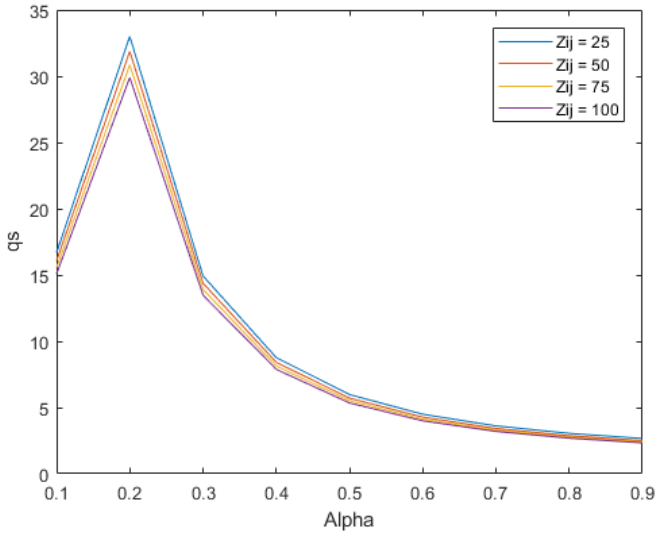

(b) Loaded Qs values for the coupling factor values shown in Fig.3.21(a)

Figure 3.21: Modeling the influence of the added transmission line to the resonator model where $l_{ij} = 2$ mm, $C_f = 0.9$ pF and $C_{ij} = 0.5$ pF

adds to the filter and the inductance the packaging adds. The model value can be found on the data sheet provided by the manufacturer [20]. The inductance added is approximately 0.7 nH and the loss is represented by a 0.8 Ω resistance. For the rest of this report the varactor capacitance values are represented as C_{f1}, C_{f2} C_{f3} and C_{ij}.

Fig. 3.22 shows that using the coupling structure adds an additional insertion loss pole between 5 and 6 GHz. Under ideal conditions the zero and pole can be seen far enough from the pass-band. However, later in Sec. 3.3.2.1 it is shown that adding the non-ideal varactor models shifts these reflections elements closer to the pass-band.

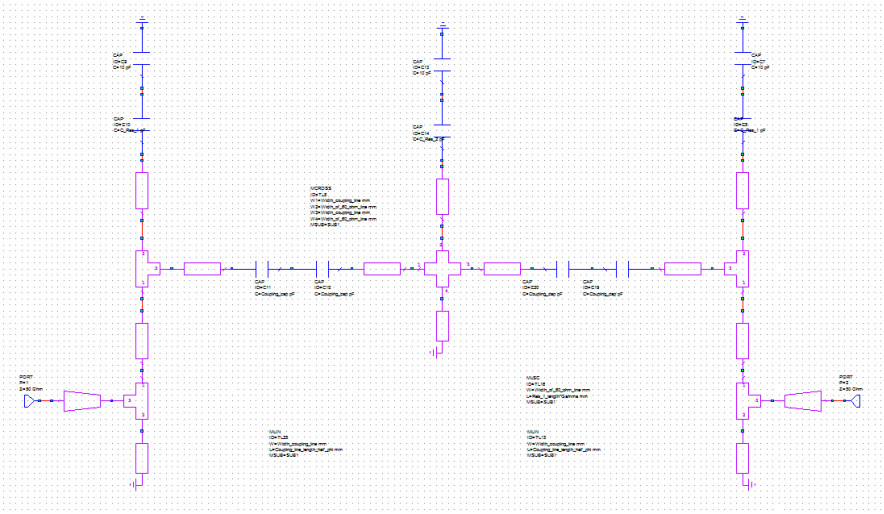

(a)

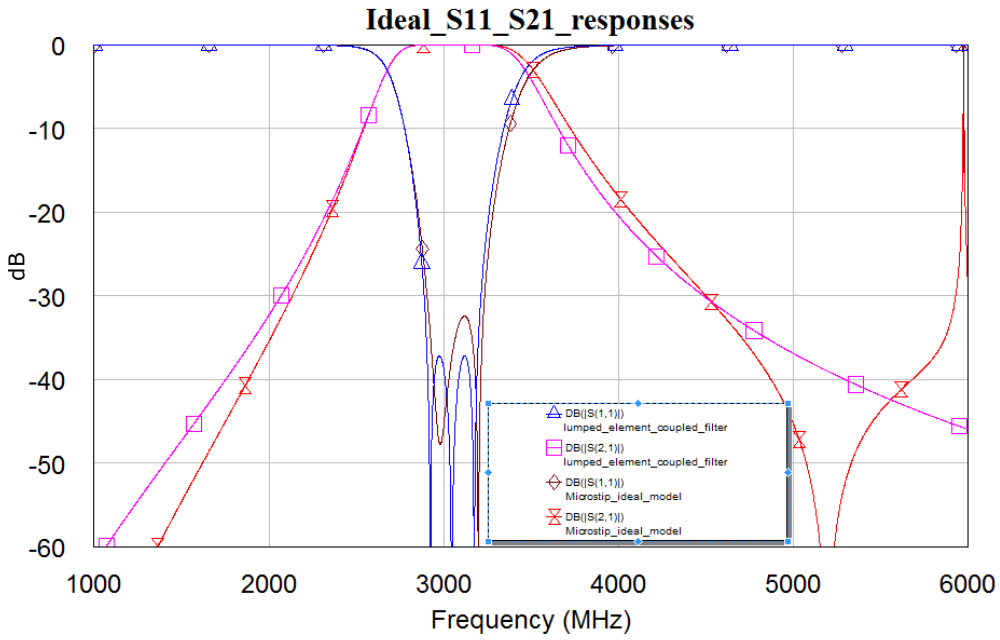

(b)

Figure 3.22: Third order AWR Microstrip Filter

3.3.2.1 AWR Test for Continuous Tuning

Continuous tunability of a constant bandwidth over 1 GHz is desired. Both S_{11} and S_{21} in Fig. 3.23 show how the filter can be shifted from the center frequency of 2.2 GHz to 3.6 GHz with the bandwidth remaining constant by changing C_{ij} and C_f. Due to the design choice of not implementing a method of controlling the source and load transformation, the quality of the pass-band response decays as the center frequency is shifted further from the original design frequency.

The simulation shows that the tunablity range in Fig. 3.23 can be achieved with the capacitance range of the varactor. The corresponding capacitance values used for the different tuned option are provided in Table 3.2. The table also provides the maximum values for S_{11} and S_{21} within

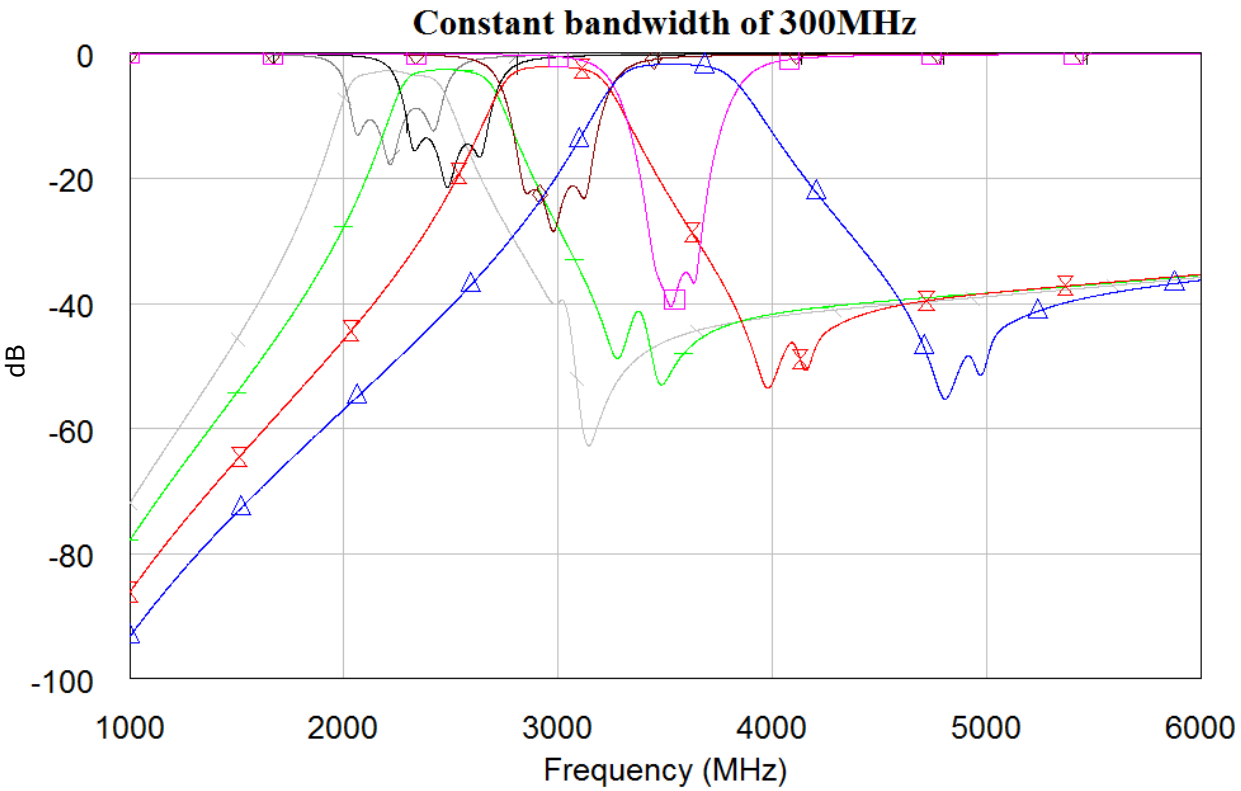

Figure 3.23: Constant 300 MHz Bandwidth

the simulated pass-bands.

Table 3.2: Band-pass measurements of Fig. 3.23

Center Frequency [GHZ]	$C_{f1}[pF]$	$C_{f3}[pF]$	$C_{f2}[pF]$	$C_{ij}[pF]$	$S_{21}[dB]$	$S_{11}[dB]$
3.535	0.85	0.85	0.83	0.8	-1.7	-35
2.971	1.27	1.27	1.27	1.15	-2.1	-21
2.476	1.95	1.95	2	1.72	-2.5	-13
2.218	2.5	2.5	2.5	2.26	-2.7	-8

The results show that the loss increases as the filter center frequency is shifted down. The increase in loss is due to the varactor, but dielectric material and conductor losses can also have an influence. With each bandwidth measurement shown in Fig. 3.23 the transmission zero and pole is shown to shift down in frequency as the value of C_{ij} is increased.

The results shown in Fig. 3.24 confirms that using a longer coupling structure transmission line is effectively the same as using a larger capacitance. This also supports the transmission line model findings from earlier simulations presented in Sec. 3.3.2. The length previously named l_{ij}, which determines the distance from the tapping point to the first varactor, also determines the placement of the reflection pole and zero. This test was done using the non-ideal varactor model, which means that even when the transmission line length is zero the inductance added

to the filter creates the peaks shown in the results. Therefore the use of a transmission line can be used to mitigate the negative attributes of using a varactor structure.

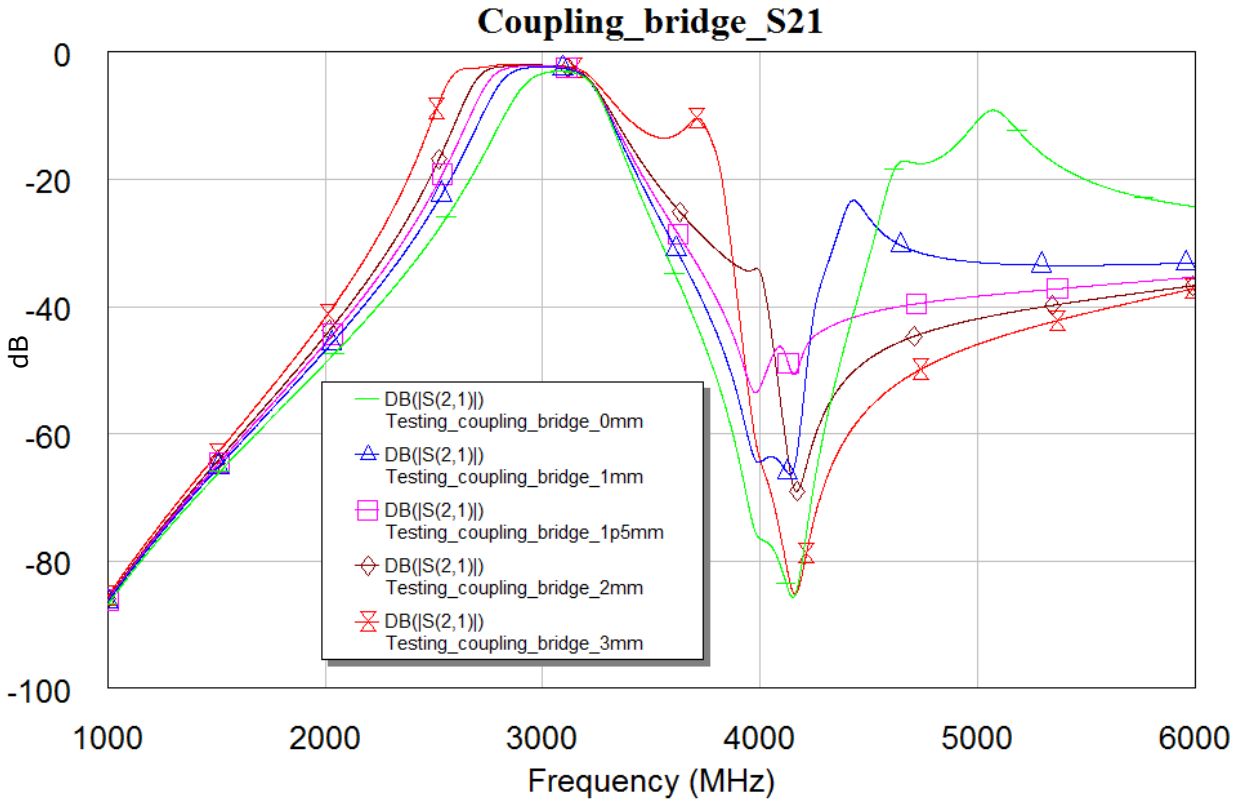

Figure 3.24: Determining the accuracy of the relationship between coupling strength and coupling structure transmission line length established in the ideal transmission line model

The results in Fig. 3.25 show that the transmission line impedance does not improve the coupling as the previous model showed. Instead the increase in coupling strength was due to the transmission pole and zero being shifted close enough to influence the pass-band. The results show that as line impedance increases the coupling structure transmission zero shifts closer to the pass-band.

3.4 Bias Circuit

Varactors are operated with external DC biasing voltages. Therefore, DC power sources must be connected to the filter to provide a voltage difference to for controlling the varactors. Biasing circuitry is typically used to isolate the DC power sources from high frequency signals so that there is minimal energy leakage from the filter. For this project, the biasing circuit should have minimal effect on the filter response and footprint.

Two circuit designs are considered for this project. Fig. 3.26(a) shows a bias circuit using a radial stub with a quarter wavelength transformation that transforms the lower impedance of the radial stub to a extremely large impedance for a specific frequency. Fig. 3.26(b) shows a biasing circuit that uses an inductor to provide a high impedance over a large bandwidth. The

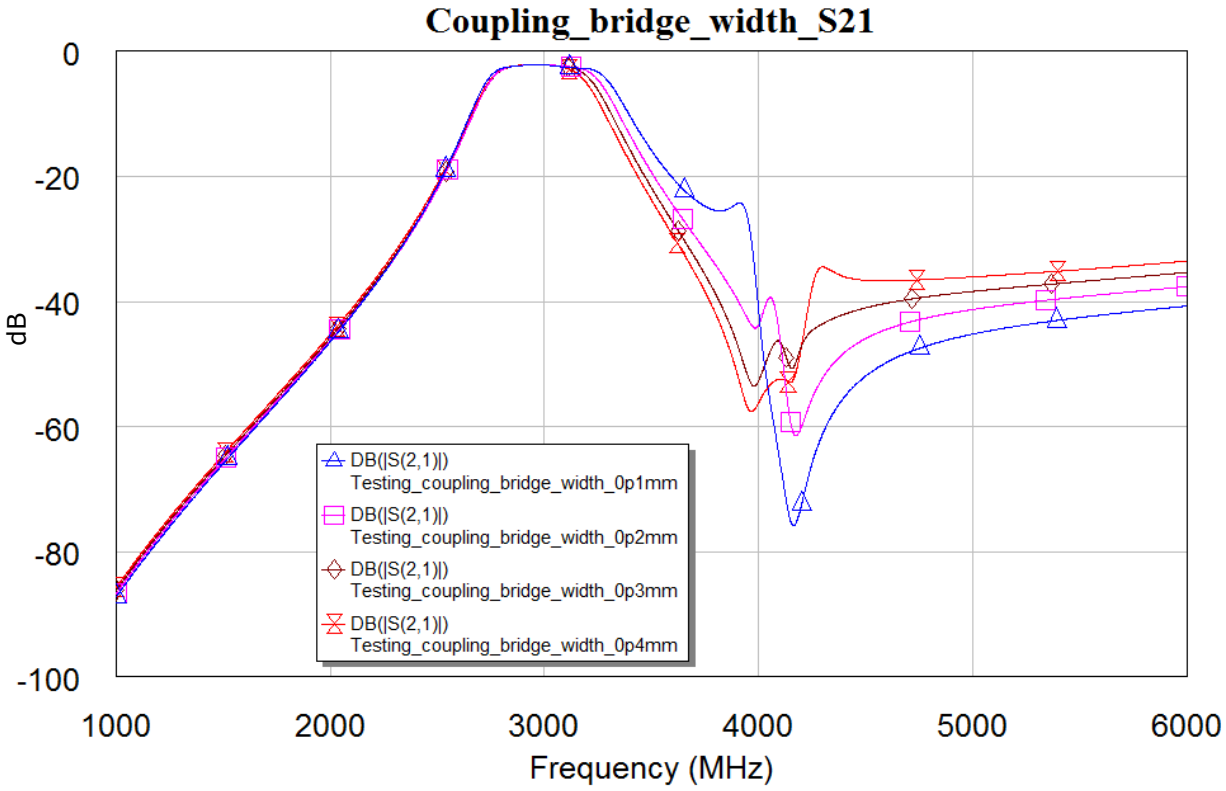

Figure 3.25: Determining the accuracy of the relationship between coupling strength and coupling structure transmission line impedance established in the ideal transmission line model

model used was provided by TDK MLK series data sheet were all necessary data was provided to setup an accurate model. The different circuits both provide a high impedance to reflect as much energy as possible.

The radial stub circuit is a very large structure relative to the inductor circuit. The inductor circuit is generally a simpler circuit to implement and provides a gradual increase in the impedance value until it approaches its Self Resonant Frequency(SRF). The SRF is the point where the package capacitance and the inductor creates a resonator. This has to be taken into account and the SRF must be above the frequency range.

To ensure that the bias circuit does not affect the filter, both bias circuits are implemented in AWR so that the circuit interaction can be determined. The results shown in Fig. 3.28(a) compares the 3rd order filter with the radial stub circuit and without. The results show that due to the frequency sensitivity of this biasing circuit it would be unsuitable for a filter that aims for a wide tuning range.

On the other hand, the inductor circuit provides an impedance that is stable over a wide bandwidth and can easily be implemented. As indicated by the results in Fig. 3.28(b) the inductor influences the filter response but is the best choice of the two options presented when considering stability over the entire operating band.

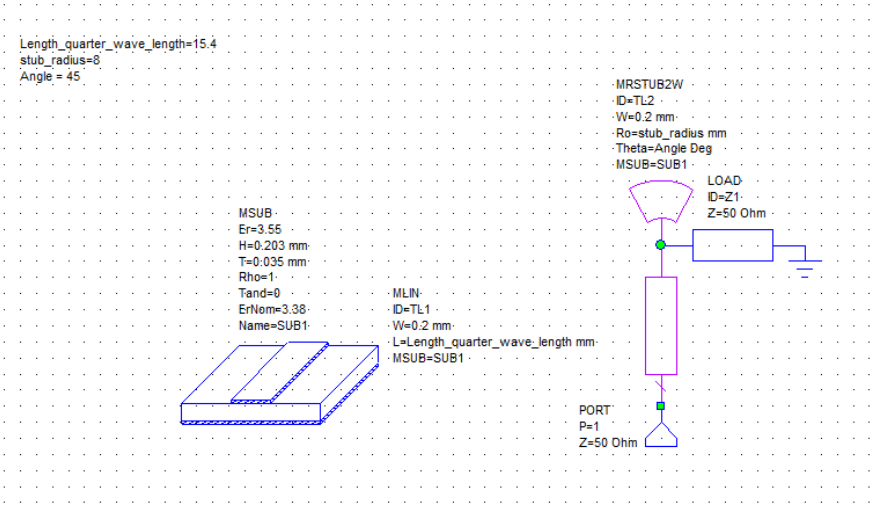

(a) Radial stub quarter wave length transformation

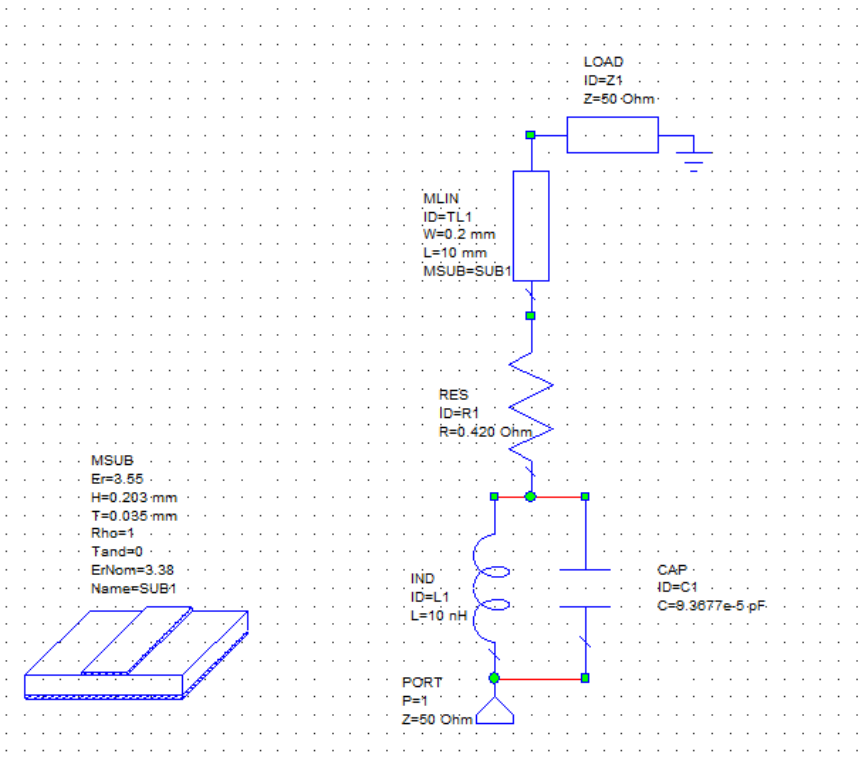

(b) Inductor element

Figure 3.26: Bias circuit layout

3.5 CST Modeling

Using the model made in AWR as a reference, the filter is implemented in CST to ensure model accuracy. This section discuses the reasoning behind modeling methods and implementation.

3.5.1 Simulation Setup

Using the frequency domain solver of CST the background material is set to vacuum. To limit the volume CST has to compute, the boundary conditions are set to an electric wall that touches the design at all sides except the side with the transmission lines. The electric wall

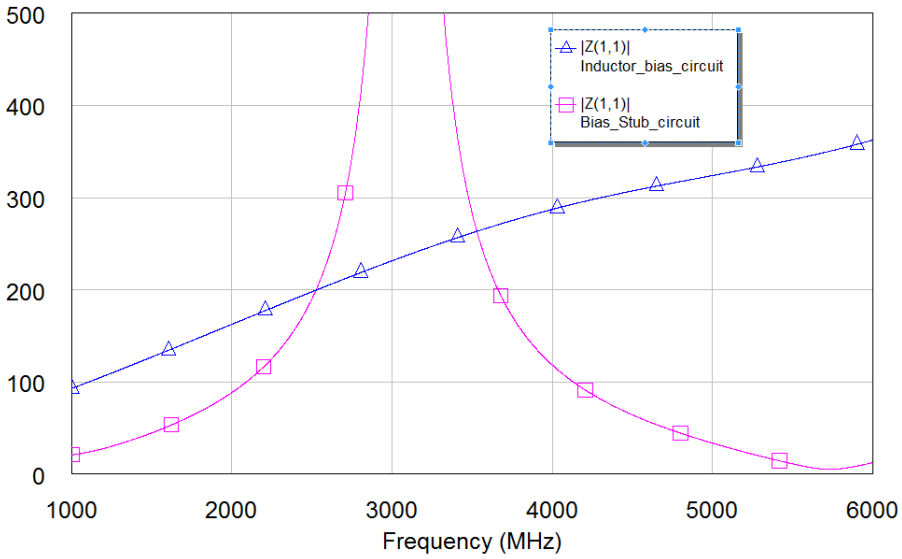

Figure 3.27: Bias Circuit Impedance

on the side where the microstrip filter is positioned is shifted so that a vacuum gap provides a space large enough to allow the simulation results without the interference from the boundary conditions or higher order modes which may be generated in the cavity.

Using the filter model in AWR as a reference, a filter model is setup in CST. To implement tunablity for this model, a discrete port is implemented to provide a point to connect circuit elements to the extracted S-parameter block.

The discrete port setup shown in Fig. 3.29 is used to provide two connection points for components to be connected between. Each component requires a discrete port for each leg of the component. In the case of Fig. 3.29 where two components have connected to the same biasing pad the discrete port can be shared thus reducing the total number of ports.

After adding the ports for the biasing circuit and input and output port , 27 ports are present in the simulation model. Fig. 3.30 gives the layout and how the ports are distributed on the filter. The schematic shown in Fig. 3.31(a) is how the full wave simulation results are used and how the components are connected to the extracted S-parameter of the filter.

The response of the filter shown in Fig. 3.31(b) shows the filter modeled using 0.203 mm thick dielectric. The original reasoning for working on this dielectric was to keep the effective dielectric constant as low as possible. This would allow the resonators to be longer and allow for a greater variety of coupling structure placements. Additionally, with all the capacitance added to the circuit, the length was already 4 mm with the 0.203 mm dielectric.

The peak shown in Fig. 3.31(b) between 5.5 and 6 GHz is a box resonance in the CST model and does not influence the filter response.

3.6 Manufacturable 3D Filter Prototype Model

The dielectric used for this design is the 0.508 mm thick Rogers RO4003C, due to difficulties of working with the thinner substrate. A thicker dielectric increase the effective dielectric constant,

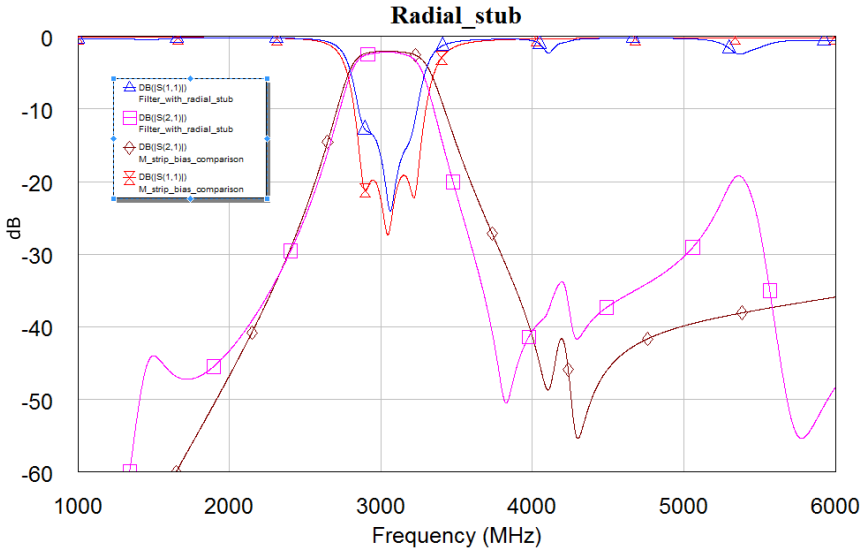

(a) Radial stub quarter wave length transformation

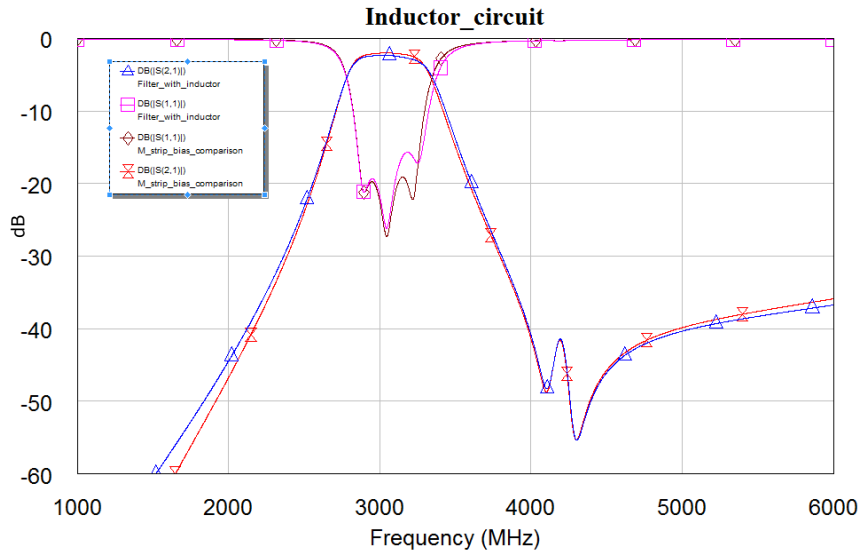

(b) Inductor element

Figure 3.28: Bias circuit implementation

meaning that the physical lengths of the transmission lines is shorter than the thinner dielectric. The line width also change as the resonator is now further from ground and the capacitance is reduced. To maintain a constant 60 Ω transmission line width changed from the 0.33 mm to 0.83 mm and to maintain the center frequency at 3.0463 GHz, the resonator length is reduced from 4 mm to 3 mm. Any additional reduction in length risks complication to the manufacturing of the filter. The coupling structure transmission line is changed to have a length and width of 1 mm and 0.3 mm. The alpha value is adjusted to 0.48 mm to achieve the required coupling strength.

The filter design for the thicker substrate is shown in Fig. 3.32 uses a C_1 and C_3 of 0.9 pF, C_2 of 0.76 pF and a C_{12} of 0.97 pF. The initial design choice to allow the filter to have a tuning range above 3.05 GHz is preserved.

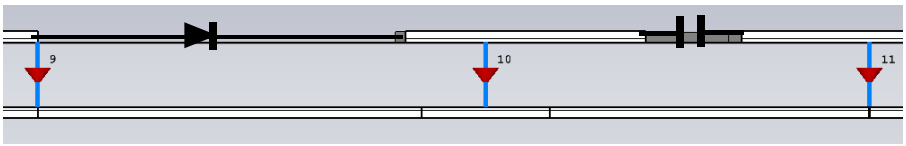

Figure 3.29: CST Discrete Port implementation

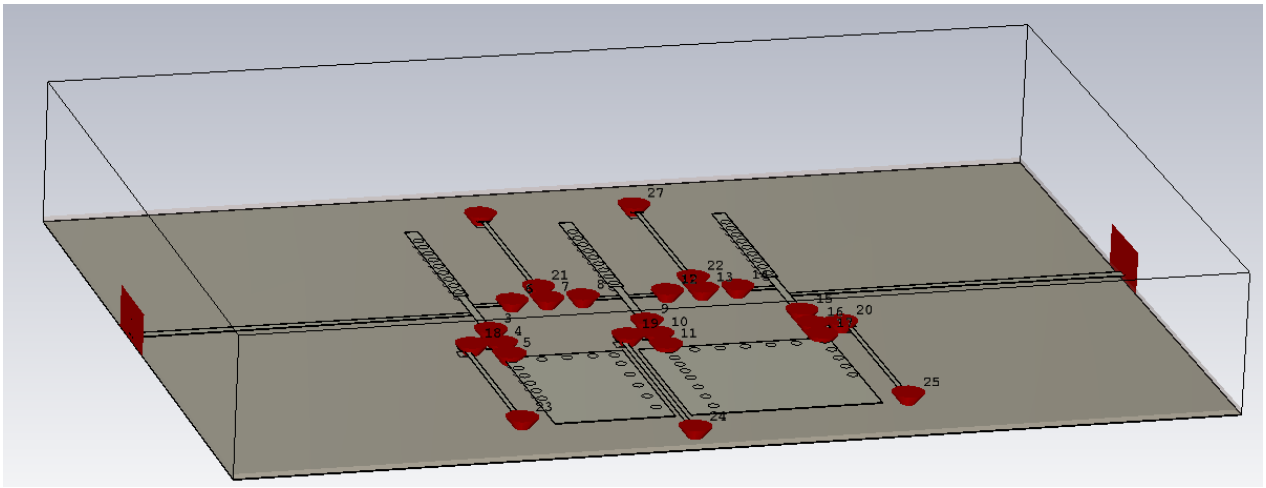

Figure 3.30: CST Simulation with Discrete Ports

The results in Fig. 3.33 shows, that within the varactor capacitance range the required filter range is achieved. The capacitance values are shown in Table 3.3 which also includes the varactor values for Fig. 3.32. The $|S_{11}|$ results in Fig. 3.33 show that as the filter is shifted down in frequency the lack of load adjustment increases the $|S_{11}|$ in the pass-band.

The upper limit of the tuning range is limited by the lower limit of C_{12}. Due to the center resonator, any adjustments to the response has a large influence on the center resonator. In order to reduce the influence on the centre frequency without compromising coupling strength, an alpha value of 0.47 is used.

Due to the capacitance sensitivity of the filter a majority of the varactor tuning range is used to shift the centre frequency in the lower frequency range.

$$k = \frac{\omega_0 C_{12}}{\sqrt{b_1 b_2}} \tag{3.6.1}$$

Additionally the growth in the required coupling factor due to the increase of the fractional pass-band as the center frequency is shifted down, due to the relationship stated in $k_{ij} = \frac{\Delta}{\sqrt{g_i g_j}}$. Larger coupling structure capacitance values are required for the lower frequencies in order to maintain constant bandwidth during centre frequency tuning.

It is important to note that the reflection zero created by the coupling structure is sensitive to the capacitance value C_{12}, meaning that as the center frequency is shifted down and a constant

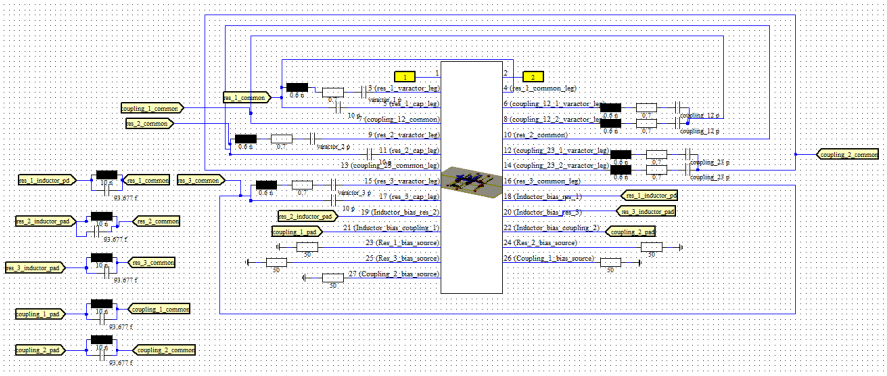

(a)

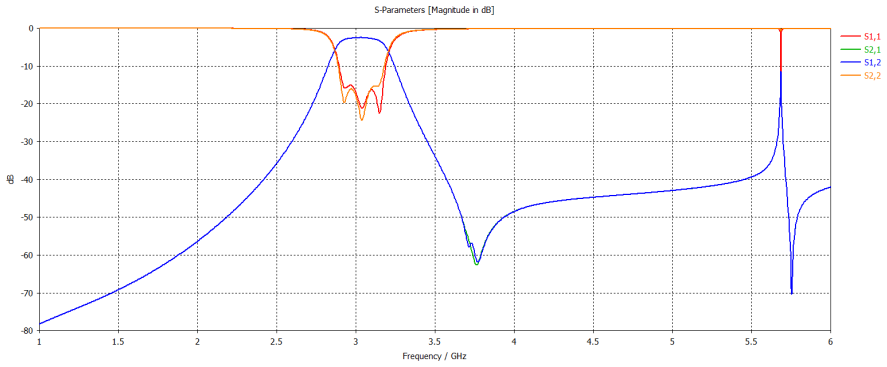

(b)

Figure 3.31: CST full circuit schematic and corresponding S parameters

Table 3.3: 300MHz band-pass CST measurements

Center Frequency [GHZ]	C_{f1}	$C_{f3}[pF]$	$C_{f2}[pF]$	$C_{ij}[pF]$
3.336	0.79	0.63	0.727	0.79
3.048	0.907	0.76	0.907	0.97
2.389	1.517	1.23	1.527	1.71

pass-band is maintained, the pole is shifted closer to the pass-band, as shown in Fig. 3.34. For this model the pole is designed so that within the the initial 1 GHz tuning range, there is no influence by the pole in the pass-band. This was achieved through trial and error.

3.7 Conclusion

In this chapter, several investigations were presented to determine the effect of the chosen varactor coupling structure, frequency tuning component, and biasing circuitry on the resonant frequency and coupling strength for different line impedances. The results from these investigations were used in the design of a filter which includes biasing circuitry and realistic varactor models. It was shown that using a high impedance transmission line allows for a wider tuning range but also increases the influence the coupling structure has over the resonant frequency of the resonator. The use of a short transmission line reduces the magnetic coupling between adjacent resonators must be taken into account. The transmission line adds some reflection poles and zeros. The line length was shown to increase the effective capacitance used in the coupling structure and additionally the placement on the resonator also can be used design the

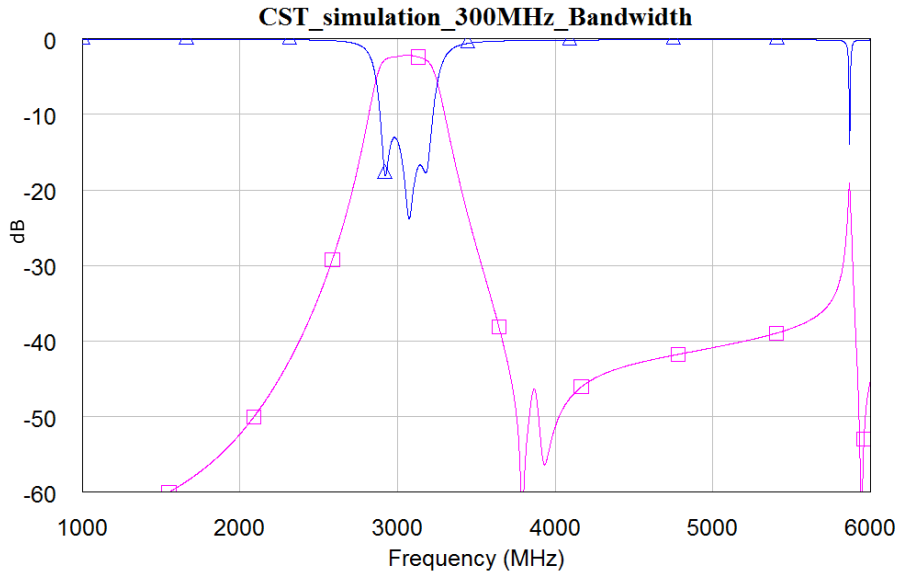

Figure 3.32: 300MHz band-pass filter center frequency 3.05GHz

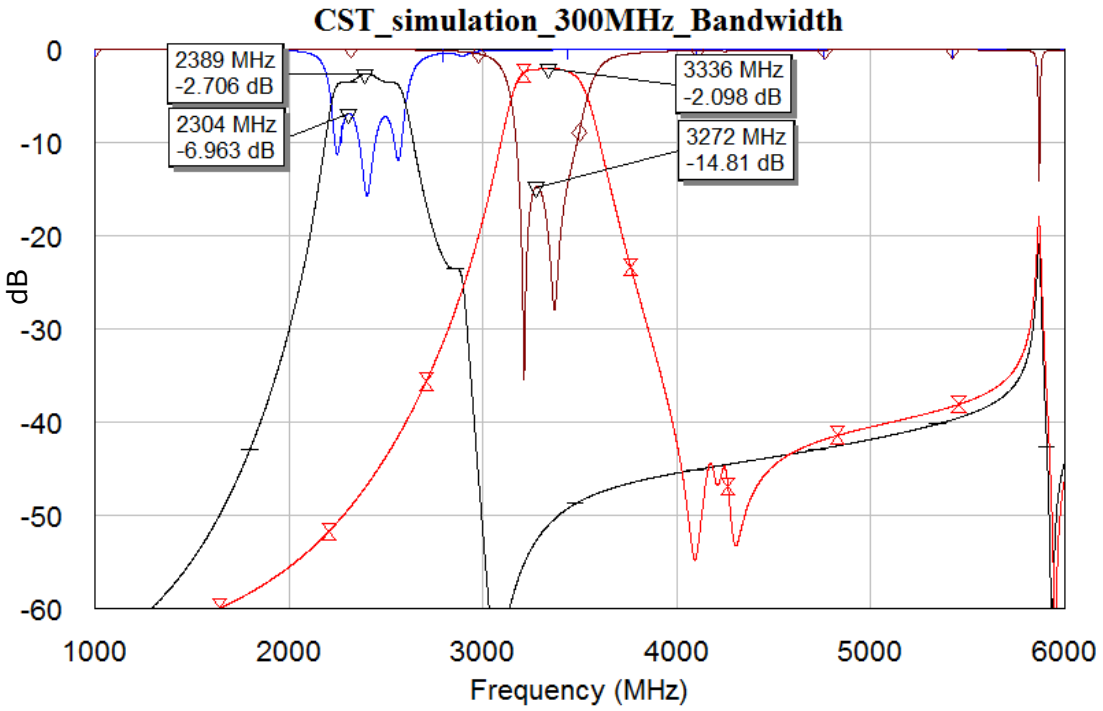

Figure 3.33: Maximum and minimum 300 MHz pass-bands achieved with the 0.508 mm substrate filter model

coupling strength. Using the characteristics shown by the AWR and transmission line model a CST model that achieves the objective of 1 GHz of tunablity with a constant bandwidth.

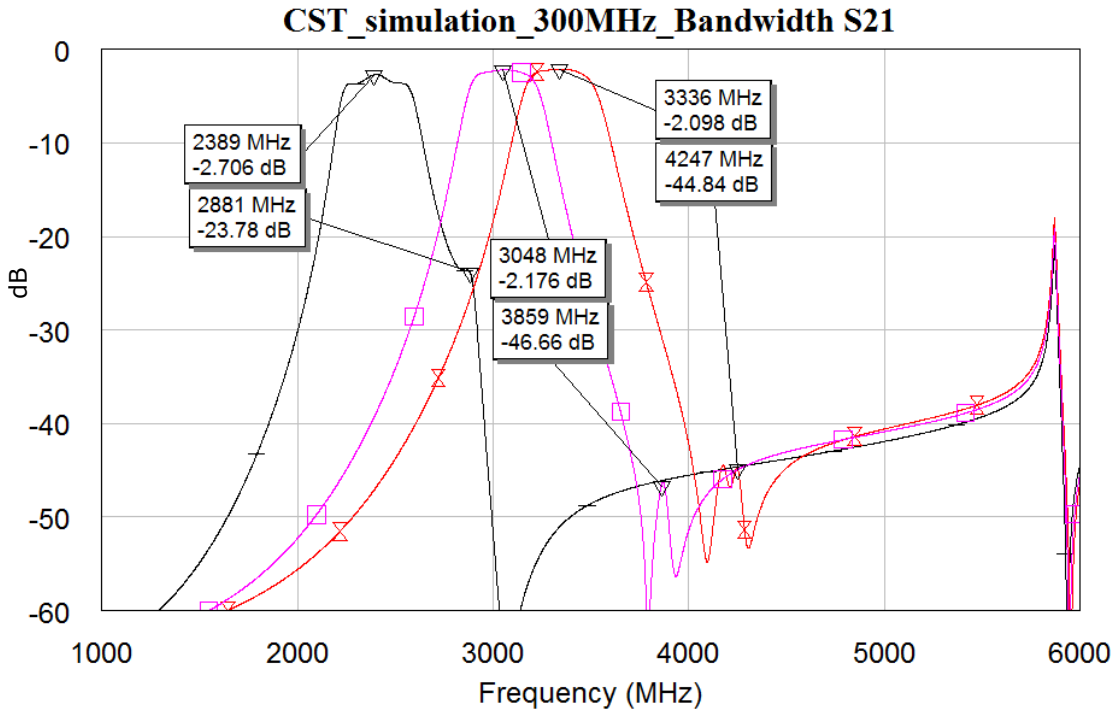

Figure 3.34: S_{21} response of the 0.508 mm substrate filter with a constant 300 MHz pass-band

Chapter 4

Manufacturing and Measurements

This chapter covers the production process and measured response of the manufactured bandwidth and frequency tunable microstrip filter.

4.1 Filter production

Milling was used to create the microstrip transmission lines from the double-sided copper clad dielectric substrate. This method was chosen due to the in-house availability of a milling machine at Stellenbosch University. One problem with milling is the risk of the drill bit milling away more than intended and decreases structure definition. The initial attempt to create the 0.203 mm Rogers RO4003CC substrate filter was too difficult due to the substrate being thin. When milling goes deeper than intended, the structural integrity of the board is decreased. The substrate is too thin and soft for the milling process. The substrate in Fig. 4.1 is the 0.203 mm

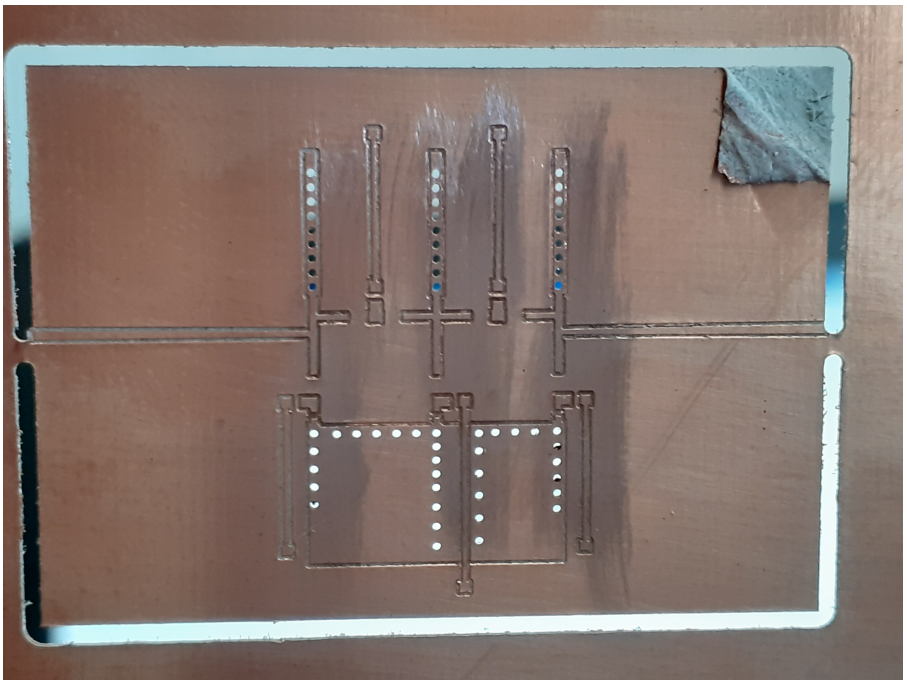

Figure 4.1: Milling of 0.203 mm Rogers dielectric

thick substrate and shows that the substrate is soft enough to cause milling issues, like milling

too deep and removing too much material. The milling of the thicker 0.508 mm substrate proved to be more successful. The advantage of using an thicker substrate in production is that the material is more rigid and does not bend in the production process. When implementing the SMA connectors it can be soldered onto the board directly and the substrate can support the weight. The thinner substrate would need a support structure that would mount the connector and support the filter weight.

The via implementation is done using wire that fits the via hole as tight as possible and soldered on both ends. This proved to be an good method of connecting all the ground layers due to the amount of vias used in the filter.

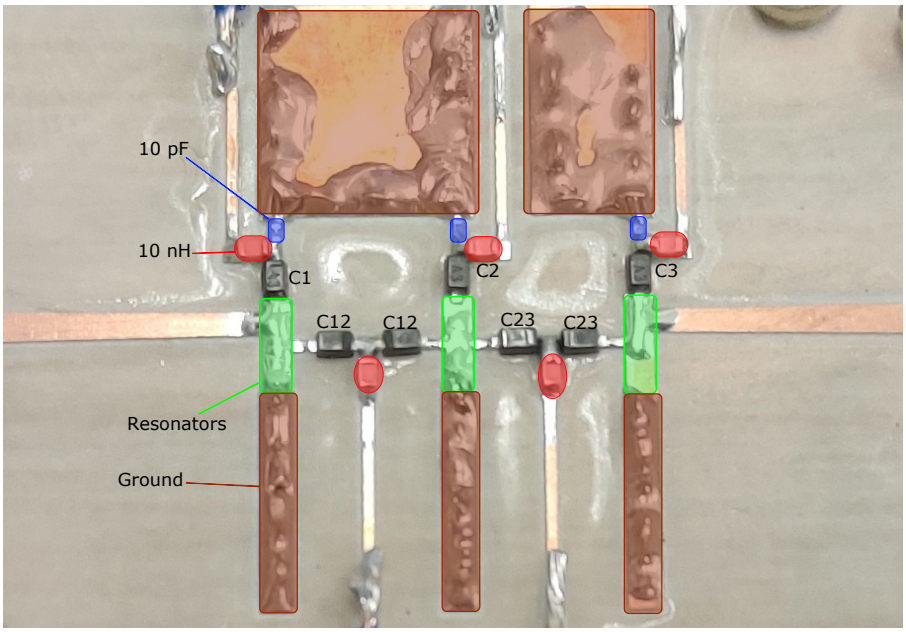

Figure 4.2: Rogers 0.508mm filter

The via placement close to the 10 pF fixed capacitor pad made the management of the excess solder difficult. This is the same when soldering the wire at the shorted end of the resonators. After soldering the wires, removing any excess solder from the filter is difficult due to the ground plane acting as a heat sink. For further designs alternative via placement will improve the ease of production. The soldering pads can also be improved in future designs so that attaching all the components can be easier by placing the inductors further from the varactor structures. Soldering all 3 components onto the pads did prove to be difficult.

4.2 Measurements and result interpretation

The filter testing was done on an Agilent Technologies PNA-X network analyser that can accurately measure from 10 MHz-26 GHz. The Network Analyzer was set to measure two port S-parameters for 1-6 GHz with 1001 samples. The calibration is done with an electronic calibration module. Five different power supplies are used to adjust the voltage of each varactor structure. Unlike the simulations, the varactors are not all identical due to manufacturing variations and each structure needs to be biased separately to be able to tune the filter correctly. The voltages applied are recorded and provided in Appendix A.

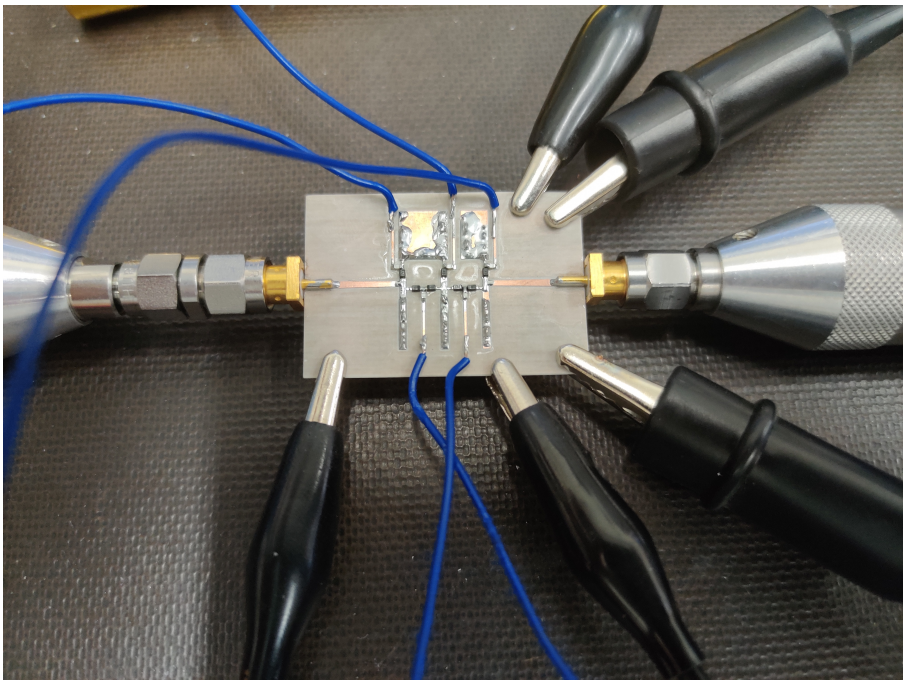

Figure 4.3: Manufactured and assembled tunable filter on 0.508 mm substrate

The filter setup is shown in Fig. 4.3. The blue wires are connected to the DC power supplies. To check that the DC power supplies are well isolated, a metal object is moved past the wire in close proximity. No affect is seen on the analyzer. The lack off response means that the amount of energies reflect due to this change in impedance is negligible meaning that the amount of energy conducted via the biasing circuit is small.

For this project the -3dB point is used to determine the pass-band, unlike the results shown in [3] and [2] which use the -1 dB points. Figure 4.4 shows 4 sets of results each with different absolute pass-bands.

The values shown in table 4.1 are the measured frequencies of each band-pass filter. The lower and upper -3 dB frequencies are represented with $f_{-3dB-low}$ and $f_{-3dB-high}$. The values of the f_0 represents the center frequency. Difficulties of obtaining exact pass-band values are due to tuning resolution of the voltage regulators. This is cause of the anomaly seen in the 300MHz data set. The data set represented in the data table represents the measured filter responses that are seen as valid, meaning that the S_{21} and S_{11} forms a valid pass-band.

Figure 4.6 shows that good agreement is achieved between measured and simulated results with the exception of the increase in insertion loss in the measured case. This difference is attributed to the varactor diode models used, and a device model extraction process should be used in future to determine a more accurate varactor model for simulation.

Using one of the pass-band as an example the loss increased by 2.8 dB which is almost half of the total expected output power. To achieve the same amount of loss in the simulations as shown in the measurements, the loss in the varactors must be increased from 0.8 Ω to 1.8 Ω which is a 225% more loss than initially anticipated. Fig. 4.7 shows how with an improved model the S21 response can significantly improve the accuracy of the model.

When comparing the measured and simulated results (Fig. 4.7) of the wider pass-bands, it is

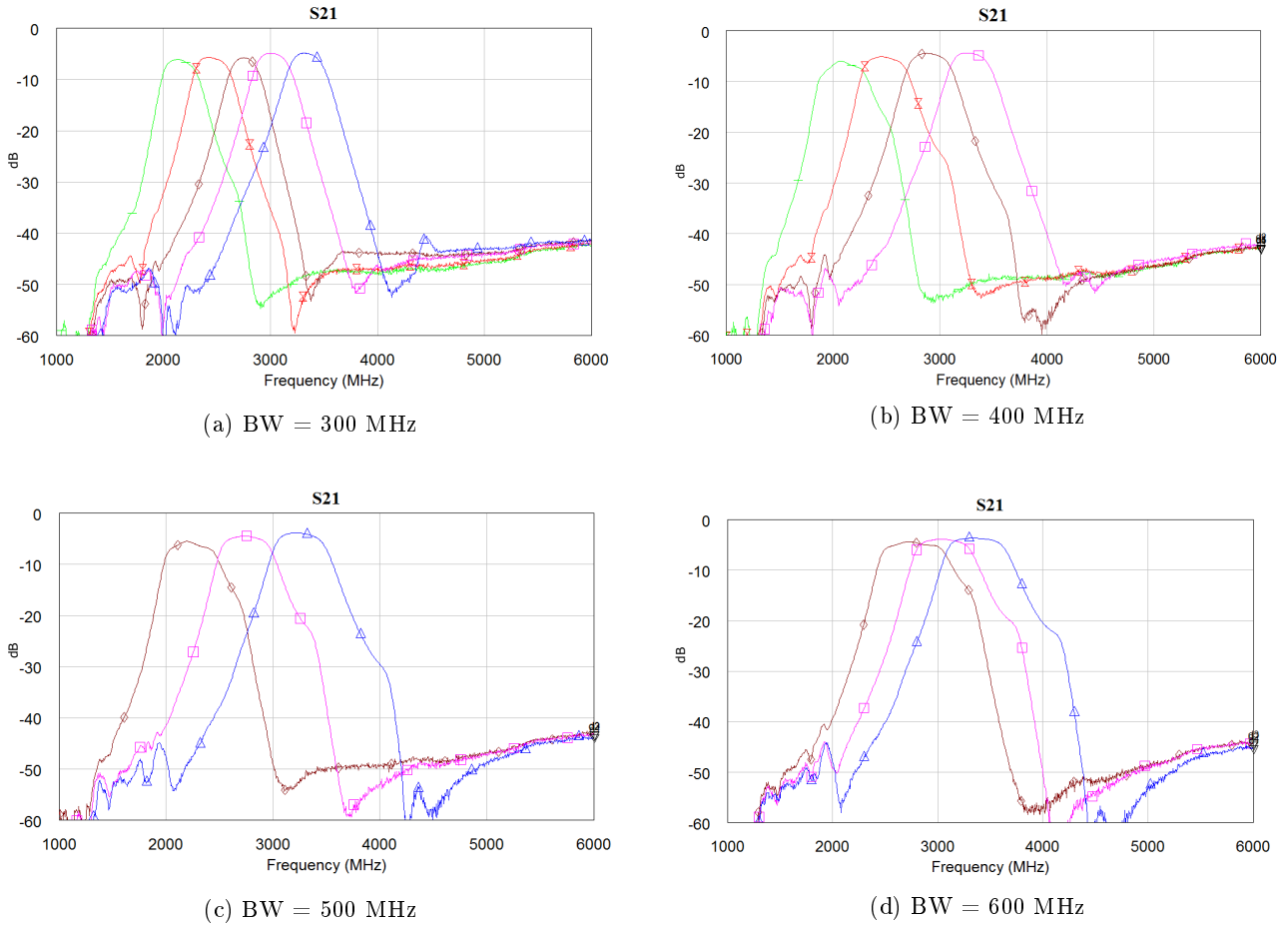

(a) BW = 300 MHz

(b) BW = 400 MHz

(c) BW = 500 MHz

(d) BW = 600 MHz

Figure 4.4: Constant bandwidth center frequency sweep with 100MHz interval increase

shown that the measured results have better responses than the simulated filter when comparing the rise of the S_{11} in the pass-band. The simulated results predicted that the source and load transformation would cause the S_{11} to not dip as deep as the measurement. Meaning that the loaded q remains in an acceptable range for longer that the model predicted.

Testing some alternative changes it was realised that the source and load transformation is extremely sensitive and any combination of taper width alteration can cause a significant influence on the pass-band. The improvement shown is the indication of the milling machine not removing enough material and accidentally improving the filter performance. Additionally modeling is not perfect and some deviation of the results can be attributed towards modeling error.

4.3 Conclusion

The measurement taken of the manufacture filter prototype showed that the influences the varactor coupling structure has on the filter response and the tuning range of the filter is accurately predicted in simulation. The increase of loss in the measured response is as a result of the varactors. The lack of tunablity of the source and load did present it self as a limiting factor by reducing the usability of pass-bands further away from the initial tuning.

Table 4.1: Measured results

Set	$f_{-3dB-low}$ GHz	$f_{-3dB-high}$ GHz	f_0 GHz	Bandwidth (%)	$\|S_{21}(f_0)\|$ dB
300MHz	3.174	3.501	3.33	9.8	-4.89
	2.857	3.183	3.02	10.81	-4.923
	2.619	2.892	2.75	9.92	-5.747
	2.29	2.623	2.45	13.59	-5.75
	1.995	2.316	2.15	14.93	-6.106
400MHz	3.094	3.472	3.28	11.53	-4.382
	2.67	3.104	2.89	14.06	-4.459
	2.275	2.693	2.48	16.89	-5.173
500MHz	3.011	3.494	3.24	14.89	-3.846
	2.507	2.987	2.74	17.54	-4.423
600MHz	3.08	3.664	3.36	17.38	-3.636
	2.781	3.333	3.04	18.131	-3.814
	2.459	3.086	2.75	22.76	-4.322

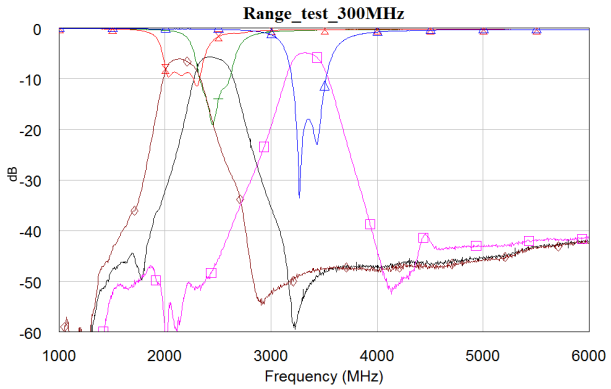

(a) 300MHz

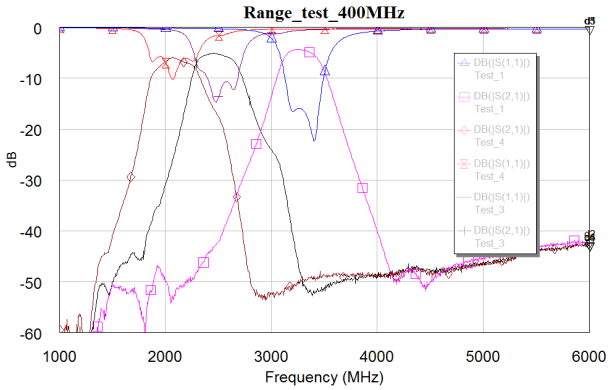

(b) 400MHz

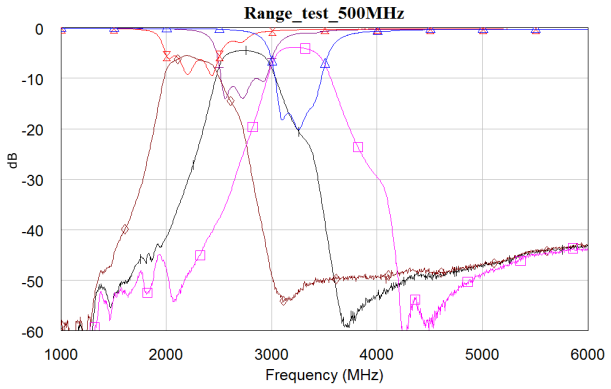

(c) 500MHz

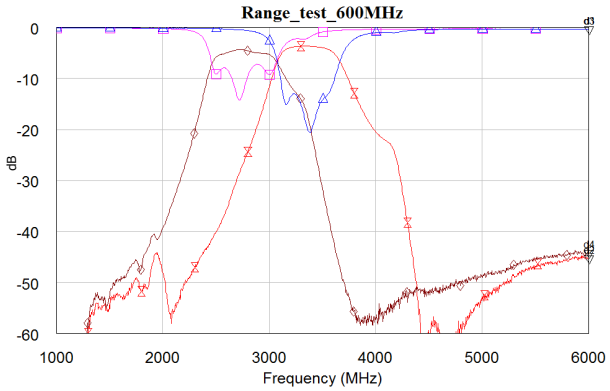

(d) 600MHz

Figure 4.5: S_{11} and S_{21} response to show the de-tuning of the source and load transformation

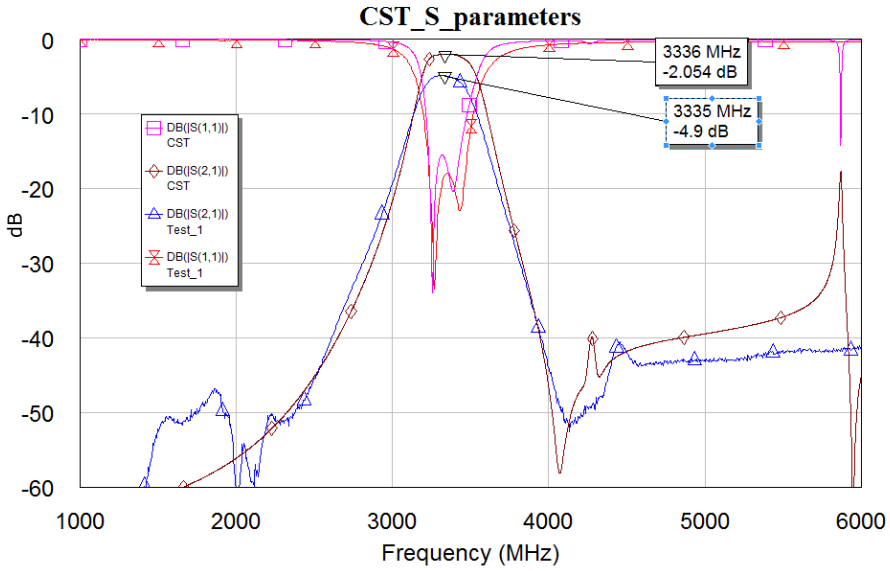

Figure 4.6: CST simulation vs measured results

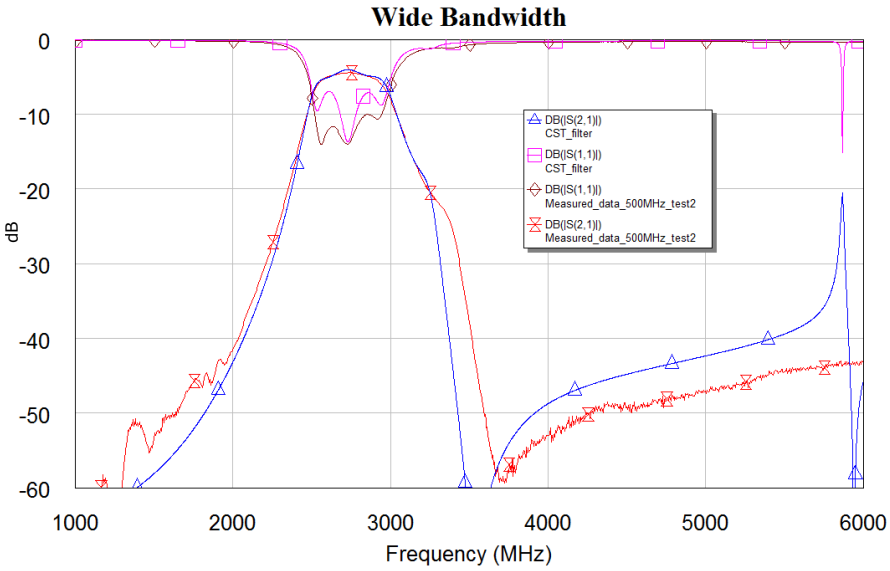

Figure 4.7: Measured data vs. simulated for wide-band measurement

Chapter 5

Conclusions and Recommendations

A requirement of the modern communication systems is the ability to adapt under changing standards and system requirements. Designing a system to with flexibility has the potential to extend a system's life span. This project focuses on the implementation of a coupling structure to provide a method of controlling the coupling strength between adjacent filters. This allows the filter to adapt as needed within the tuning range of the filter.

Using the simulation and bi-variant analysis the influence of the coupling structure, presented in this project, has on a filter. The placement of the coupling structure showed the coupling coefficient can vary from approximately 0 to 0.26 depending on the transmission line impedance. The placement bi-variant studies also showed that the increase of alpha also determines the how much of an influence the coupling structure has on the resonant frequency of the connected resonators.

The initial AWR models showed that the initial assumptions that the transmission line added to the coupling structure would not affect the pass-band is wrong. Said line introduced both an insertion loss zero and pole to the filter response. The AWR model showed that the insertion loss pole was not affected by the varactor values and could be manipulated by the value of alpha. The insertion loss zero showed an extreme sensitivity towards the varactor's capacitance value and as the structure is used to increase the coupling strength the zero moved closer and closer the pass-band. The measured data shows that when testing the widest pass-bands the pole was shown to affect the roll-off rate of the pass-band. Additional studies showed that the transmission line of the coupling structure also increased the influence the varactor has on the coupling strength and resonant frequency.

The coupling structure showed through simulation, and corroborated experimentally, that the coupling structure provided a method that can maintain multiple sets of pass-bands that range of 300 and 600 MHz with a center frequency tuning range of 3.33 to 2.12 GHz and 3.36 to 2.75 GHz. Due to limitations of varactor ranges maintaining larger bandwidths reduced the center frequency tuning range. This achieved the initial goal of maintaining a constant bandwidth for at least 1 GHz. With these requirements met this design has the potential to be functional when considering the cost and simplicity of design, but due to the insertion loss zero added to the response maintaining a pass-band unaffected is difficult. Unlike the filter design shown by [1] the zero could not be placed far enough from the pass-band. Additional issues for this filter design is the lack of source and load transformations that are critical to maintaining a good pass-band over a large tuning range, but due low loaded q of the first and last resonator it was

shown to be difficult to implement anything other than a direct connection between source and load.

It is recommended that the next step of this research can be the use of mediums like suspended substrates and similar filter types to reduce the effective dielectric constant so that the coupling structure can be applied on the higher frequencies. Use of a higher accurate model for varactors to take loss into account and use lower loss varactos in future designs. The use of components like MEMS and components with low losses can also be investigated for the use of creating a filter version that has a better response. A future hybrid between the T-type(shown in [3]) coupling structure and the one used in this project may prove to be able to achieve an highly versatile filter design. Investigate methods to implement of source and load transformations to maintain better pass-bands.

Bibliography

[1] S. K. Sharma, "Variable bandwidth planar coupled resonator filters utilizing tunable non-resonant node inverters," 2018.

[2] Y. Chiou and G. M. Rebeiz, "A tunable three-pole 1.5-2.2-ghz bandpass filter with bandwidth and transmission zero control," *IEEE Transactions on Microwave Theory and Techniques*, vol. 59, no. 11, pp. 2872–2878, 2011.

[3] P. Chi, T. Yang, and T. Tsai, "A fully tunable two-pole bandpass filter," *IEEE Microwave and Wireless Components Letters*, vol. 25, no. 5, pp. 292–294, 2015.

[4] J.-S. Hong, *Microstrip Filters for RF/Microwave Applications*. Wiley Series in Microwave and Optical Engineering, Hoboken: Wiley, 2nd ed. ed., 2010.

[5] G. Matthaei, L. Young, and E. Jones, *Microwave filters, impedance-matching networks, and coupling structures*. Dedham, Mass.: Artech House, 1980.

[6] I. Skyworks Solutions, *VARACTOR DIODES*, 2020.

[7] R. Levy and S. B. Cohn, "A history of microwave filter research, design, and development," *IEEE Transactions on Microwave Theory and Techniques*, vol. 32, no. 9, pp. 1055–1067, 1984.

[8] A. C. Guyette, "Intrinsically switched varactor-tuned filters and filter banks," *IEEE Transactions on Microwave Theory and Techniques*, vol. 60, no. 4, pp. 1044–1056, 2012.

[9] A. S. Hussaini, R. Abd-Alhameed, and J. Rodriguez, "Tunable rf filters: Survey and beyond," in *2011 18th IEEE International Conference on Electronics, Circuits, and Systems*, pp. 512–515, 2011.

[10] G. M. Rebeiz and J. B. Muldavin, "Rf mems switches and switch circuits," *IEEE Microwave Magazine*, vol. 2, no. 4, pp. 59–71, 2001.

[11] L. P. B. Katehi, G. M. Rebeiz, and C. T. . Nguyen, "Mems and si-micromachined components for low-power, high-frequency communications systems," in *1998 IEEE MTT-S International Microwave Symposium Digest (Cat. No.98CH36192)*, vol. 1, pp. 331–333 vol.1, 1998.

[12] E. Meyer, "Tunable narrow-band x-band bandpass filters," 2018.

[13] Byung-Wook Kim and Sang-Won Yun, "Varactor-tuned combline bandpass filter using step-impedance microstrip lines," *IEEE Transactions on Microwave Theory and Techniques*, vol. 52, no. 4, pp. 1279–1283, 2004.

[14] R. Levy, R. V. Snyder, and G. Matthaei, "Design of microwave filters," *IEEE Transactions on Microwave Theory and Techniques*, vol. 50, no. 3, pp. 783–793, 2002.

[15] D. M. Pozar, *Microwave engineering*. MTT002, 4th ed. ed., 2012.

[16] S. Caspi and J. Adelman, "Design of combline and interdigital filters with tapped-line input," *IEEE Transactions on Microwave Theory and Techniques*, vol. 36, no. 4, pp. 759–763, 1988.

[17] E. G. Cristal, "Tapped-line coupled transmission lines with applications to interdigital and combline filters," *IEEE Transactions on Microwave Theory and Techniques*, vol. 23, no. 12, pp. 1007–1012, 1975.

[18] G. L. Matthaei, "Interdigital band-pass filters," *IRE Transactions on Microwave Theory and Techniques*, vol. 10, no. 6, pp. 479–491, 1962.

[19] Y.-C. Chiou and G. M. Rebeiz, "A tunable three-pole 1.5-2.2-ghz bandpass filter with bandwidth and transmission zero control," *IEEE Transactions on Microwave Theory and Techniques*, vol. 59, no. 11, pp. 2872–2878, 2011.

[20] I. Skyworks Solutions, *SMV1405 to SMV1430 Series: Plastic-Packaged Abrupt Junction Tuning Varactor*, 2008.

Appendices

Appendix A

Table 1: Varactor Voltage measurements

Set	V_{12}	V_{23}	V_1	V_2	V_3
300MHz	13.9	12.5	11.8	19.8	11.6
	7.8	7.1	7.1	11.4	6.7
	4.9	5.0	3.6	6.6	4.1
	1.9	2.0	1.9	3.2	1.5
	0.7	0.5	0.5	1.6	0.6
400MHz	10.7	10.6	10.9	19.1	11.3
	4.4	4.8	5.1	11.9	5.7
	1.6	1.6	2.1	4.6	2.2
500MHz	8.1	8.1	11.2	22.1	10.1
	2.9	2.7	4.4	9.6	3.9
600MHz	8.6	8.6	14.2	30.4	12.6
	5.0	4.8	7.9	17.7	7.9
	2.2	2.2	5.1	11.2	4.4